Industrial
Chemistry
& Materials

ROYAL SOCIETY
OF CHEMISTRY

REVIEW

View Article Online
View Journal

Check for updates

Cite this: DOI: 10.1039/d5im00116a

2D catalysts for assisted water electrolysis: mechanistic insights and theoretical perspectives for industrial hydrogen generation

Hyojung Lim,†[a] Seonghyeon Park,†[a] Jinuk Choi, †[a] Junho Shim,[a]
Subramani Surendran [a] and Uk Sim *[ab]

The efficiency of conventional water electrolysis is fundamentally constrained by the sluggish kinetics and high overpotential of the oxygen evolution reaction (OER). Assisted water electrolysis has emerged as a promising strategy to overcome this limitation by replacing OER with the selective oxidation of small organic or nitrogen-containing molecules such as urea, ammonia, methanol, ethanol, glycerol, and formic acid. These alternative anodic reactions offer significantly lower thermodynamic oxidation potentials, thereby enabling hydrogen production at reduced cell voltages while simultaneously achieving pollutant remediation and value-added chemical synthesis. Two-dimensional (2D) materials have garnered increasing attention as efficient catalysts for oxidation reactions in assisted water electrolysis, owing to their unique structural and electronic properties. This review summarizes recent progress in 2D catalysts, including layered double hydroxides, transition metal dichalcogenides, MXenes, metallenes, and graphene-based materials, emphasizing their roles in facilitating various oxidation reactions. Key strategies, including doping, defect engineering, and interface modulation, are discussed in relation to enhancing catalytic activity, selectivity, and durability. Thermodynamic analyses and Pourbaix diagrams are introduced to provide insight into the reaction pathways and stability windows of both feedstocks and catalysts under various electrochemical conditions. By integrating rational catalyst design with a comprehensive understanding of various oxidation reactions, assisted water electrolysis using 2D catalysts offers a compelling pathway toward sustainable hydrogen production. The co-benefits of improved energy efficiency and environmental sustainability position this approach as a promising solution to current energy and environmental challenges. Developing 2D materials and understanding reactions are expected to accelerate the implementation of next-generation electrolysis systems aligned with global carbon neutrality goals.

Received 24th June 2025,
Accepted 24th September 2025

DOI: 10.1039/d5im00116a

rsc.li/icm

Keywords: 2D catalysts; Assisted water electrolysis; Hydrogen generation; Pourbaix diagrams; Density functional theory (DFT).

1 Introduction

1.1 Importance of assisted water electrolysis

With the urgency of phasing out fossil fuels, electrochemical water electrolysis has gained prominence as a sustainable pathway for hydrogen production. Unlike thermochemical methods that rely on hydrocarbons, water electrolysis offers a carbon-free approach that can be directly powered by renewable electricity.[1–3] This eliminates greenhouse gas emissions at the source and enables decentralized hydrogen generation. However, the overall water electrolysis process is energetically demanding due to the sluggish oxygen evolution reaction (OER), which not only requires a high overpotential but also suffers from poor selectivity and stability in practical conditions.[4–7] To address these limitations, assisted water electrolysis strategies have garnered significant attention.[8–12] By replacing the OER with alternative oxidation reactions involving small organic or nitrogen-containing molecules, the overall energy input can be substantially reduced. These assisted oxidation reactions typically exhibit lower theoretical oxidation potentials and faster kinetics compared to OER, enabling more energy-efficient hydrogen production and coupled chemical synthesis.

Moreover, assisted water oxidation not only enables the conversion of pollutants such as ammonia (NH_3), hydrazine (N_2H_4), and urea ($CO(NH_2)_2$) into non-toxic products, but also facilitates the synthesis of value-added products like formic acid

---

[a] Hydrogen Energy Technology Laboratory, Korea Institute of Energy Technology (KENTECH), Naju, Jeonnam 58330, Republic of Korea. E-mail: usim@kentech.ac.kr
[b] Research Institute, NEEL Sciences, Inc., Naju, Jeonnam 58326, Republic of Korea

† These authors contributed equally to this work.

(HCOOH) from methanol (CH_3OH) and glycerol ($C_3H_8O_3$).[13–17] Therefore, selecting appropriate oxidation substrates and understanding their electrochemical behavior are crucial for designing effective assisted water electrolysis systems.

1.2 Types of assisted water electrolysis

Various small molecules, including ammonia, hydrazine, urea, methanol, ethanol, and formic acid, have been explored as anodic substrates to replace the oxygen evolution reaction (OER) in water electrolysis (Fig. 1). Each of these species exhibits distinct electrochemical behavior depending on the pH, applied potentials, and thermodynamic properties. The ammonia oxidation reaction (AOR) produces N_2, which can exist in either the gas or aqueous phase.[18] The standard electrode potential (E^0) of the reaction varies slightly depending on the phase of the N_2 product. In addition, the speciation of the ammonia reactant depends on the solution pH, governed by the acid–base equilibrium of $NH_4^+ \rightleftarrows NH_3 + H^+$, with a p$K_\alpha$ value of 9.251 under standard conditions (25 °C, 1 atm). Consequently, the AOR pathway differs depending on the phase states of both NH_3 and N_2, as illustrated in the following half-reactions (eqn (1)–(4)):[19,20]

$$2NH_4^+ \rightleftharpoons N_2(g) + 8H^+ + 6e^-, \quad E^0 = 0.275 \text{ V } vs. \text{ SHE} \tag{1}$$

$$2NH_4^+ \rightleftharpoons N_2(aq) + 8H^+ + 6e^-, \quad E^0 = 0.306 \text{ V } vs. \text{ SHE} \tag{2}$$

Hyojung Lim

Hyojung Lim is a doctoral student in the Hydrogen Energy Technology Laboratory at the Korea Institute of Energy Technology (KENTECH), Republic of Korea. She earned her B.S. in Chemistry and Energy Engineering from Sookmyung Women's University in 2022 and her M.S. from KENTECH in 2025. Her research focuses on electrochemical ammonia synthesis and water splitting for sustainable energy applications.

Seonghyeon Park

Seonghyeon Park is a master's student in the Hydrogen Energy Technology Laboratory at the Korea Institute of Energy Technology (KENTECH), Republic of Korea. He received his B.S. in Chemistry from Pukyong National University. His research focuses on the design and development of electrocatalysts for green ammonia production.

Jinuk Choi

Jinuk Choi is a doctoral student in the Hydrogen Energy Technology Laboratory at the Korea Institute of Energy Technology (KENTECH), Republic of Korea. He earned his B.S. and M.S. degrees in Materials Science and Engineering from Chosun University (2019) and Hanyang University (2021), respectively. His research focuses on the electrochemical synthesis of ammonia and urea under ambient conditions.

Uk Sim

Prof. Uk Sim is an Associate Professor in the Hydrogen Energy Technology Laboratory at the Korea Institute of Energy Technology (KENTECH), Republic of Korea. He earned his B.S. (2007), M.S. (2009), and Ph.D. (2016) in Materials Science and Engineering from Seoul National University. Following his doctoral studies, he completed a postdoctoral fellowship at Stanford University in 2017. He later served as an Associate Professor in the Department of Materials Science and Engineering at Chonnam National University. In addition to his academic roles, he is the Founder and CEO of Neel Sciences Inc., a research institute. His research focuses on the design and development of nanomaterials for energy production, conversion, and storage, with particular emphasis on renewable energy systems based on photo- and electrochemical reactions aimed at building a sustainable energy future.

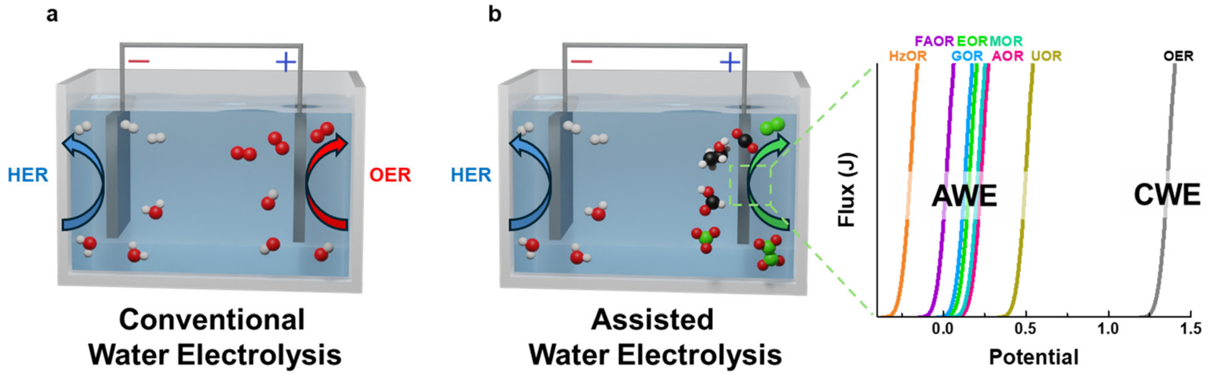

Fig. 1 Schematic illustration of (a) conventional water electrolysis (OER-HER) and (b) assisted water electrolysis, where various anodic reactions (AOR, UOR, MOR, EOR, FAOR, HzOR) replace the OER.

$$2NH_3(aq) + 6OH^- \rightleftharpoons N_2(g) + 6H_2O(l) + 6e^-, \quad E^0 = 0.092\ \text{V}\ \mathit{vs.}\ \text{SHE} \tag{3}$$

$$2NH_3(aq) + 6OH^- \rightleftharpoons N_2(aq) + 6H_2O(l) + 6e^-, \quad E^0 = 0.123\ \text{V}\ \mathit{vs.}\ \text{SHE} \tag{4}$$

Urea is a major pollutant commonly found in wastewater and has been utilized as a feedstock for assisted water electrolysis.[21] The theoretical potentials of the urea oxidation reaction (UOR) have been extensively investigated due to the relatively complex nature of the reaction, which involves multi-electron transfer and consideration of the product phases. The UOR proceeds according to the following half-reaction (eqn (9)):[22,23]

$$CO(NH_2)_2(aq) + 6OH^- \rightleftharpoons N_2(g) + CO_2(g) + 5H_2O(l) + 6e^-, \quad E^0 = 0.072\ \text{V}\ \mathit{vs.}\ \text{SHE} \tag{5}$$

Hydrazine, commonly found in industrial wastewater, has also been widely investigated as an anodic feedstock for assisted water electrolysis.[24] Similar to the AOR, the standard electrode potentials of the hydrazine oxidation reaction (HzOR) depend on the pH of the electrolyte and the physical phase of the N_2 product. The acid–base equilibrium of hydrazine is governed by the reaction $N_2H_5^+ \rightleftarrows N_2H_4 + H^+$, with a p$K_\alpha$ value of 8.10 under standard conditions.[25] Accordingly, the thermodynamic driving force for HzOR varies based on the protonation state of hydrazine and the phase of the N_2 produced, as illustrated in the following half-reactions (eqn (5)–(8)):[26]

$$N_2H_5^+ \rightleftharpoons N_2(aq) + 5H^+ + 4e^-, \quad E^0 = -0.167\ \text{V}\ \mathit{vs.}\ \text{SHE} \tag{6}$$

$$N_2H_5^+ \rightleftharpoons N_2(g) + 5H^+ + 4e^-, \quad E^0 = -0.214\ \text{V}\ \mathit{vs.}\ \text{SHE} \tag{7}$$

$$N_2H_4(aq) + 4OH^- \rightleftharpoons N_2(aq) + 4H_2O(l) + 4e^-, \quad E^0 = -0.284\ \text{V}\ \mathit{vs.}\ \text{SHE} \tag{8}$$

$$N_2H_4(aq) + 4OH^- \rightleftharpoons N_2(g) + 4H_2O(l) + 4e^-, \quad E^0 = -0.332\ \text{V}\ \mathit{vs.}\ \text{SHE} \tag{9}$$

The theoretical potential of the methanol oxidation reaction (MOR) is influenced by both the pH of the electrolyte and the nature of carbon-containing intermediates or products.[27] Typically, a standard potential of 0.016 V *vs.* SHE is used for methanol oxidation in direct methanol fuel cells.[28] However, under aqueous conditions relevant to assisted water electrolysis, the thermodynamic properties of methanol differ. The MOR proceeds through multi-electron transfer steps, ultimately leading to the formation of CO_2. The corresponding half-reactions are summarized as follows (eqn (10)–(12)):[29,30]

$$CH_3OH(l) + H_2O(l) \rightleftharpoons CO_2(g) + 6H^+ + 6e^-, \quad E^0 = 0.016\ \text{V}\ \mathit{vs.}\ \text{SHE} \tag{10}$$

$$CH_3OH(aq) + H_2O(l) \rightleftharpoons CO_2(g) + 6H^+ + 6e^-, \quad E^0 = 0.032\ \text{V}\ \mathit{vs.}\ \text{SHE} \tag{11}$$

$$CH_3OH(aq) + H_2O(l) \rightleftharpoons CO_2(aq) + 6H^+ + 6e^-, \quad E^0 = 0.046\ \text{V}\ \mathit{vs.}\ \text{SHE} \tag{12}$$

Furthermore, MOR can potentially yield value-added chemicals such as formic acid. The theoretical potential for the partial oxidation pathway ($CH_3OH \rightarrow HCOOH$, $E^0 = 0.103$ V *vs.* SHE) is thermodynamically slightly less favorable than the complete oxidation to CO_2 ($E^0 = 0.046$ V *vs.* SHE). Although CO_2 remains the most stable end-product, the selective formation of HCOOH is kinetically accessible under suitable catalysts and reaction conditions, thereby offering an opportunity for co-generation of chemicals alongside hydrogen. The CH_3OH-to-HCOOH pathway is summarized as follows (eqn (13)):

$$CH_3OH(aq) + H_2O(l) \rightleftharpoons HCOOH(aq) + 4H^+ + 4e^-, \quad E^0 = 0.103\ \text{V}\ \mathit{vs.}\ \text{SHE} \tag{13}$$

Similarly, the ethanol oxidation reaction (EOR) exhibits multiple pathways depending on the reaction conditions and the nature of the final products.[31] A standard potential of 0.084 V *vs.* SHE for ethanol oxidation is widely referenced in the field of direct ethanol fuel cells.[32] However, under aqueous conditions relevant to assisted water electrolysis, the thermodynamic behavior of ethanol differs. Therefore, the aqueous phase of both reactants and products should be considered for accurate potential calculation. The consideration of phase transitions between reactants and products results in variations in the calculated theoretical potentials. Representative half-reactions are summarized below (eqn (14)–(16)):[30,33]

$$CH_3CH_2OH(l) + 12OH^- \rightleftharpoons 2CO_2(g) + 9H_2O(l) + 12e^-, \quad E^0 = 0.084 \text{ V } vs. \text{ SHE} \tag{14}$$

$$CH_3CH_2OH(aq) + 12OH^- \rightleftharpoons 2CO_2(g) + 9H_2O(l) + 12e^-, \quad E^0 = 0.090 \text{ V } vs. \text{ SHE} \tag{15}$$

$$CH_3CH_2OH(aq) + 12OH^- \rightleftharpoons 2CO_2(aq) + 9H_2O(l) + 12e^-, \quad E^0 = 0.105 \text{ V } vs. \text{ SHE} \tag{16}$$

Glycerol, a major organic pollutant frequently generated from biodiesel and other industrial processes, has also been widely utilized as a feedstock for assisted water electrolysis.[34] Its oxidation offers the dual benefits of energy-efficient hydrogen production and simultaneous waste valorization. The following half-reaction describes the theoretical redox potential for the glycerol oxidation reaction (GOR) (eqn (17)):[35]

$$C_3H_8O_3(l) + 3H_2O(l) \rightleftharpoons 3CO_2(g) + 14H^+ + 14e^-, \quad E^0 = 0.003 \text{ V } vs. \text{ SHE} \tag{17}$$

The formic acid oxidation reaction (FAOR) has also attracted considerable attention as an alternative anodic reaction in assisted water electrolysis due to its benefits in environmental remediation and energy efficiency.[36] As a common pollutant in various industrial waste streams, formic acid can be selectively oxidized to carbon dioxide under mild electrochemical conditions. Importantly, FAOR also exhibits a significantly lower theoretical oxidation potential compared to the OER, making it highly advantageous for reducing the overall energy input in electrolysis systems. The FAOR proceeds according to the following half-reactions (eqn (18)):[37]

$$HCOOH(aq) \rightleftharpoons CO_2(g) + 2H^+ + 2e^-, \quad E^0 = -0.114 \text{ V } vs. \text{ SHE} \tag{18}$$

The oxidation potentials were calculated using the FactSage software, excluding UOR and GOR due to the lack of thermodynamic data. These calculated potentials provide valuable guidance for predicting precise energy consumption and optimizing the system design of assisted water electrolysis.

The Pourbaix diagram provides a thermodynamic framework that maps the stable phases of reactants and products as a function of potential and pH. Such visualizations offer valuable insight into the electrochemical operation window and the prediction of possible products under given conditions. Fig. 2 presents the Pourbaix diagrams, calculated using the FactSage thermochemical software package with the FactPS database (excluding urea), for assisted water electrolysis with various molecular feedstocks.

To calculate the theoretical potentials and construct the Pourbaix diagrams, the thermodynamic reversible voltage was determined using the equation:

$$E^0 = -\Delta G^0/nF \tag{19}$$

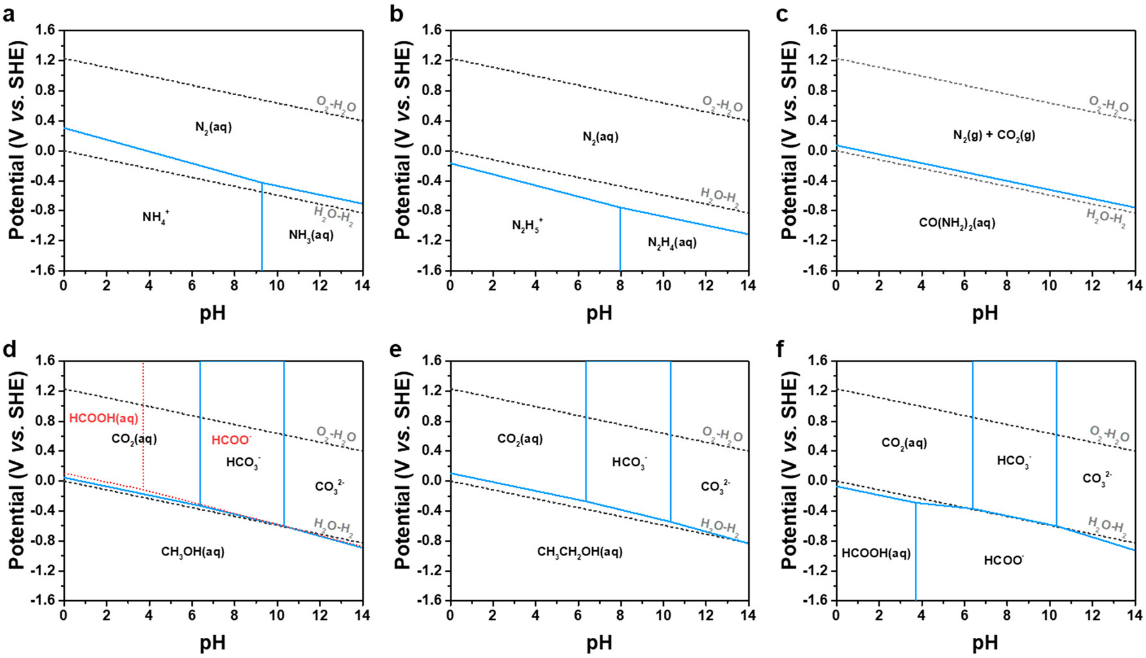

Fig. 2 Pourbaix diagrams for (a) ammonia, (b) hydrazine, (c) urea, (d) methanol, (e) ethanol, and (f) formic acid redox at 298.15 K and 1 bar.

under standard conditions. The Pourbaix diagrams were then derived using the generalized Nernst equation:

$$\alpha A + \beta B + hH^{+} + ze^{-} = \gamma C + \delta D \tag{20}$$

$$E_h = E^0 - \frac{RT\lambda}{zF}\left(\log\left(\frac{[C]^{\gamma}[D]^{\delta}}{[A]^{\alpha}[B]^{\beta}}\right) + h\text{pH}\right) \tag{21}$$

Notably, the theoretical oxidation potentials of these molecules are significantly lower than that of the conventional OER (1.23 V *vs.* RHE), thereby enabling more energy-efficient anodic processes.[38] These results of the calculations represent standard-state thermodynamics. Deviations are expected under real electrolytic environments due to concentration, ionic strength, and mass-transport effects. Nevertheless, they provide a consistent baseline for benchmarking assisted water electrolysis.

Fig. 2a illustrates the Pourbaix diagram for the AOR, where the theoretical oxidation potential remains well below that of OER across the entire pH range. Notably, a change in the slope of the potential-pH relationship is observed at pH 9.251, corresponding to the pK_α of the NH_4^+/NH_3 equilibrium. Similarly, the HzOR exhibits even lower theoretical potentials than AOR throughout the pH spectrum (Fig. 2b). As shown in the Pourbaix diagram, the slope of the potential curve shifts at pH 8.10, which corresponds to the pK_α of the $N_2H_5^+/N_2H_4$ equilibrium. These features highlight the favorable thermodynamics of HzOR and AOR for energy-saving hydrogen production through assisted water electrolysis. Similarly, UOR exhibits a low theoretical potential while generating benign products (CO_2 and N_2), making it a highly attractive anodic reaction.[39] As shown in Fig. 2c, these products remain thermodynamically stable across a wide pH range. In contrast, the potential remains significantly lower than that of OER, highlighting the advantages of UOR in reducing energy consumption and treating urea-rich wastewater.

To further understand the behavior of MOR across the entire pH range, a Pourbaix diagram for CH_3OH was constructed (Fig. 2d). The oxidation potential of MOR remains consistently below that of the conventional OER, confirming its thermodynamic advantage. Notably, the slope of the potential-pH relationship changes depending on the dominant carbonate species formed (CO_2, HCO_3^-, or CO_3^{2-}), which vary depending on pH. These shifts in product speciation influence the MOR potential, with strongly alkaline conditions exhibiting a larger potential gap between MOR and OER than acidic or neutral environments. The red dashed line indicates the kinetically accessible partial oxidation pathway ($CH_3OH \rightarrow HCOOH$), whereas the solid lines represent the thermodynamically favorable complete oxidation to CO_2. Similarly, Fig. 2e presents the Pourbaix diagram for EOR. The theoretical oxidation potential of EOR is slightly higher than that of MOR, primarily due to the presence of a C–C bond in ethanol, which requires greater energy to cleave during the oxidation process. In the case of FAOR, Fig. 2f displays an additional inflection in the potential curve resulting from the acid–base equilibrium between HCOOH and $HCOO^-$ (pK_α = 3.745). This protonation-dependent speciation results in a distinct transition in the Pourbaix diagram, further influencing the electrochemical window for FAOR operation. The thermodynamic evaluation and corresponding Pourbaix diagrams of various molecular feedstocks, including ammonia, hydrazine, urea, methanol, ethanol, glycerol, and formic acid, demonstrate their promise as viable anodic alternatives to the conventional OER in water electrolysis. Each molecule exhibits distinct pH-dependent electrochemical behavior, governed by the acid–base equilibrium and phase stability of the involved species. Notably, all of the reactions investigated exhibit significantly lower theoretical oxidation potentials compared to OER, thereby offering considerable reductions in energy input. These findings underscore the significance of selecting rational feedstocks and optimizing electrolytes in the development of high-efficiency assisted water electrolysis systems.

1.3 Types of 2D catalysts and their properties

Two-dimensional (2D) materials, defined by their atomic- or few-layer thickness, exhibit distinct structural and electronic properties that make them highly attractive for electrocatalysis.[19] Compared to 1D catalysts such as nanowires and nanotubes, which offer directional electron transport, and 3D structures like metal–organic frameworks (MOFs) or porous bulk materials that provide high loading capacity, 2D materials exhibit a unique balance of surface accessibility and electronic tunability. This dimensional contrast helps highlight the distinct advantages of 2D catalysts in electrochemical applications. 2D materials offer high surface area, abundant exposed active sites, and excellent charge transport properties.[40,41] In this review, we summarize recent advances in various 2D materials employed in assisted water electrolysis, with a particular focus on their roles and performance. Further, the electrochemical test protocols for each catalyst for their respective assisted water electrolysis are given in Table 1.

Layered double hydroxides (LDHs) and transition metal dichalcogenides (TMDs) are among the most representative and widely investigated 2D materials.[42–48] LDHs, composed of positively charged metal hydroxide layers with intercalated anions, offer abundant active sites and enable flexible compositional engineering, making them excellent candidates not only for oxygen evolution but also for alcohol oxidation reactions. NiFe-LDH and CoFe-LDH are representative examples of LDHs.[49–52] However, LDHs suffer from intrinsically low conductivity, which limits their catalytic activity. To address this, the electronic structure reconstruction of LDHs should be conducted by introducing heterostructures, forming cationic and anionic vacancies, and so on.

TMDs are layered compounds of the general formula MX_2, where M is a transition metal and X is a chalcogen (S, Se, or Te), exhibiting unique electronic, optical, and catalytic properties.[53–55] However, their catalytic activity primarily occurs at the edge sites with unsaturated dangling bonds.[56] Thanks to

Table 1 Electrochemical test protocols of each catalyst for their respective assisted water electrolysis

Reaction	Catalyst	Electrolyte	Cell system	Counter electrode	Reference electrode	Working electrode fabrication	Ref.
UOR	$MoSe_2/NiSe_2$	1 M KOH + 0.5 M urea	3-Electrode	Pt electrode	Ag/AgCl	Catalysts were grown on NF	77
	NiOOH/(LDH/α-FeOOH)	1 M KOH + 0.33 M urea	3-Electrode	Pt plate	Hg/HgO	Catalysts were grown on NF	79
	Mo-FeNi LDH	1 M KOH + 0.33 M urea	3-Electrode	Carbon rod	Hg/HgO	Ink dropping on the glassy carbon electrode	80
HzOR	NbS_2	1 M KOH + 0.5 M hydrazine	3-Electrode	Graphite rod	Ag/AgCl	Ink dropping on the glassy carbon electrode	85
	$Co(OH)_2/MoS_2/CC$	1 M KOH + 0.4 M hydrazine	3-Electrode	Pt sheet	SCE	Catalysts were grown on CC	86
	Ru_c/NiFe-LDH	1 M KOH + 0.3 M hydrazine	3-Electrode	Graphite rod	Hg/HgO	Catalysts were grown on NF	87
MOR	NiMn-LDHs	1 M KOH + 3 M CH_3OH	3-Electrode	Graphite rod	Ag/AgCl	Catalysts were grown on NF	93
	NiFe-LDH/NiFe-HAB/CF	1 M KOH + 3 M CH_3OH	3-Electrode	Pt foil	SCE	Catalysts were grown on CF	95
EOR	CoFe LDH/MoS_2/Ni_3S_2/NF	1 M KOH + 0.34 M C_2H_5OH	3-Electrode	Graphite rod	SCE	Catalysts were grown on NF	94
GOR	$Co_2[NiPcS_8]$	1 M KOH + 0.1 M glycerol	3-Electrode	Pt mesh	Ag/AgCl	Ink dropping on the carbon paper	98
	Pt_{SA}–NiCo LDH/NF	1 M KOH + 0.1 M glycerol	3-Electrode	Carbon rod	Hg/HgO	Catalysts were grown on NF	99
FAOR	B–PdCu-c/a	0.5 M H_2SO_4 + 0.5 M formic acid	3-Electrode	Pt plate	Ag/AgCl	Ink dropping on the glassy carbon electrode	100

their tunable electronic structure, TMDs allow for the modulation of catalytic behavior through layer control, doping, and defect or interface engineering, making them highly adaptable for various electrochemical reactions.[57,58] Among TMD catalysts, MoS_2, WS_2, and $MoSe_2$ have been most widely investigated for their electrochemical performance.

In addition, 2D metal–organic frameworks (MOFs) and graphitic carbon-based materials such as graphene and MXenes are also increasingly explored for their tailored structures and electronic properties.[59–63] Graphene and MXenes have been frequently combined with other materials and widely studied recently to synergistically enhance electrocatalytic performance through improved conductivity and increased exposure of active sites. For instance, MoS_2/graphene CoNi-MOF/MXene composites, Co_2FeO_4@rGO composites, $Mo_2Ti_2C_3T_x$, and Mxene-based metal oxide electrocatalysts.[64–69] Despite their advantages, carbon-based materials are prone to oxidation under harsh electrochemical conditions, which not only decreases their stability but also impairs catalytic performance.[70] Therefore, considerable efforts such as defect control, surface passivation, introduction of oxidation-resistant termination groups, and other strategies are required to enhance their overall performance.[71–73]

2 2D catalysts for urea oxidation

The urea oxidation reaction (UOR) is one of the most attractive alternative anode reactions for hydrogen generation. The UOR only requires 0.37 V *vs.* RHE, which is significantly less than the 1.23 V *vs.* RHE required for OER. Furthermore, a considerable amount of the wastewater contains urea, which provokes environmental pollution.[74,75] Therefore, if hydrogen is generated using urea derived from sewage, it is much more environmentally friendly. However, along with these advantages, UOR still faces a significant challenge due to the sluggish reaction caused by the 6-electron mechanism.[76] Thus, the catalysts with high performance are essential for the efficient generation of hydrogen.

Chen *et al.* reported a $MoSe_2/NiSe_2$ electrocatalyst for urea-assisted water electrolysis.[77] The catalyst exhibited improved conductivity and UOR activity due to the introduction of the heterostructure. As shown in Fig. 3a, the X-ray diffraction (XRD) analysis was conducted on $MoSe_2/NiSe_2$. The peaks at about $2\theta = 38.0°$, 41.9°, 47.5°, 56.4°, 76.4° correspond to (103), (006), (105), (110), and (205) crystal planes of $MoSe_2$, respectively. Similarly, the peaks at approximately $2\theta = 29.6°$, 42.4°, 50.2°, 52.6°, and 55.0° correspond to the (200), (220), (311), (222), and (023) crystal planes of $NiSe_2$, respectively. However, the peaks of $MoSe_2$ were not clearly observed due to its poor crystalline structure. To ascertain the presence of $MoSe_2/NiSe_2$ heterostructure, Raman spectroscopy was performed on $MoSe_2/NiSe_2$ (Fig. 3b). In the Raman spectroscopy, the A_g mode of $NiSe_2$ peak is located at 219.8 cm^{-1}, and the A_{1g}, E^1_{2g} modes of $MoSe_2$ peaks are located at 235.0 cm^{-1} and 286.6 cm^{-1}, respectively. Through the XRD and X-ray photoelectron spectroscopy (XPS) results, the presence of the $MoSe_2/NiSe_2$ heterostructure was confirmed. Fig. 3c shows the high-resolution X-ray photoelectron spectroscopy (XPS) spectra of Mo 3d, providing further insight into the chemical states of the composites. In the graph, the Mo $3d_{5/2}$ and $3d_{3/2}$ of Mo^{4+} were confirmed at approximately 228.26 and 231.94 eV, respectively. These characteristic Mo^{4+} peaks confirm the presence of the $MoSe_2$ structure in both samples. In addition, the Mo 3d peak of $MoSe_2/NiSe_2$ exhibits a negative shift compared with bare $MoSe_2$, which is attributed to electron transfer from Ni to Mo due to the electronegativity difference between Mo (2.16) and Ni (1.91). Through the XRD, Raman spectroscopy, and XPS results, the presence of the $MoSe_2/NiSe_2$ heterostructure was confirmed. Fig. 3d displays the linear sweep voltammetry (LSV) curve for UOR in 1 M KOH with 0.5 M urea solution. To compare the catalytic activity, the bare $MoSe_2$, $NiSe_2$, and $NiMoO_4$ were tested together. The $MoSe_2/NiSe_2$ exhibited the highest UOR activity, requiring a potential of only 1.41 V *vs.* RHE to reach a current

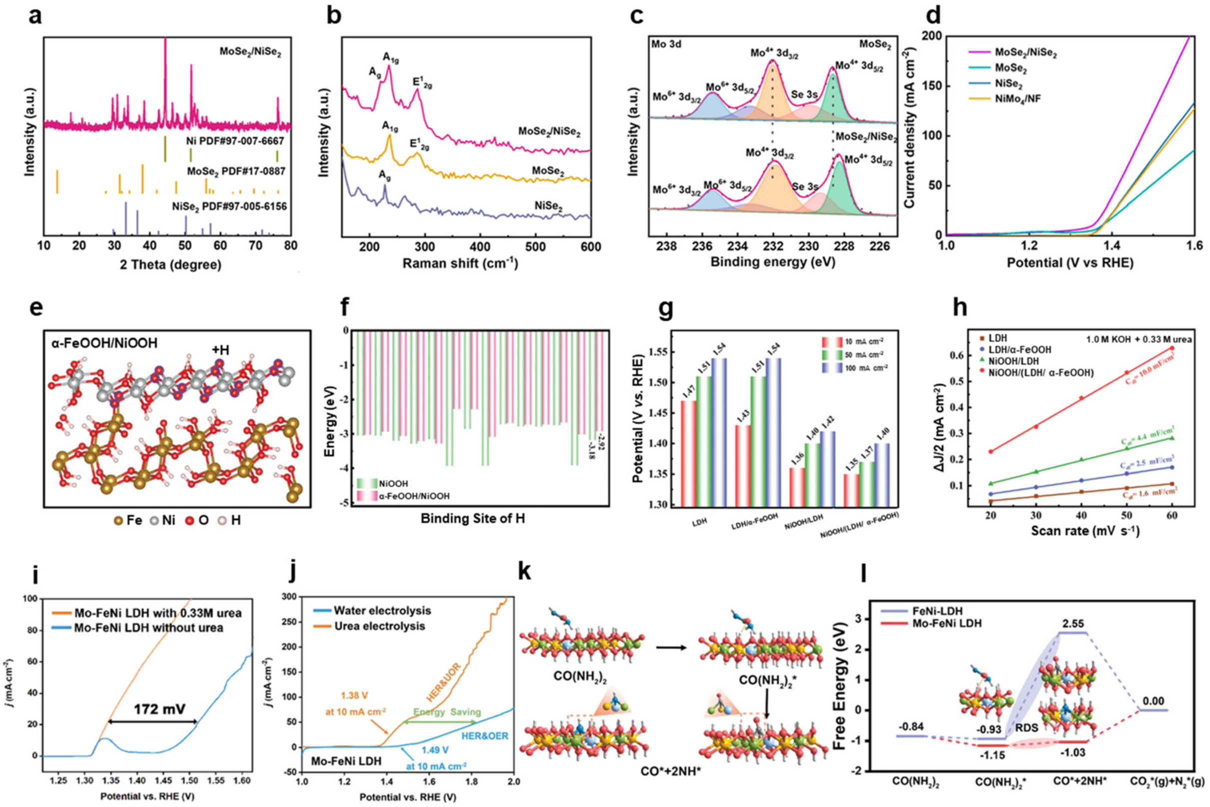

Fig. 3 Various 2D catalysts for the urea oxidation reaction. (a) XRD patterns of MoSe$_2$/NiSe$_2$, (b) Raman spectrum of MoSe$_2$/NiSe$_2$, MoSe$_2$, and NiSe$_2$, (c) Mo 3d high-resolution XPS spectra, and (d) LSV curve of MoSe$_2$/NiSe$_2$, MoSe$_2$, NiSe$_2$, and NiMoO$_4$/NF for UOR, reprinted with permission from ref. 77, copyright 2024 American Chemical Society; (e) structural model of α-FeOOH/NiOOH, (f) calculated EH value of NiOOH and α-FeOOH/NiOOH at oxygen sites, (g) required potentials at 10, 50, and 100 mA cm^{-2}, and (h) C_{dl} value of catalysts, reprinted with permission from ref. 79, copyright 2022 Wiley-VCH GmbH; (i) LSV curves of Mo-FeNi LDH for UOR and OER, (j) LSV curves comparing UOR||HER and OER||HER performance, (k) UOR mechanisms on Mo–FeNi LDH, and (l) the free-energy pathway for the UOR, reprinted with permission from ref. 80, copyright 2023 Wiley-VCH GmbH.

density of 50 mA cm^{-2}, whereas MoSe$_2$, NiSe$_2$, and NiMoO$_4$ required 1.49, 1.45, and 1.45 V *vs.* RHE, respectively. This result represents the potential for UOR using a TMD-based catalyst.

Extensive research is being conducted on NiFe-based layered double hydroxides (LDHs), which exhibit exceptional performance in oxidation reactions due to their 2D structure. This is attributed to Ni oxyhydroxide (NiOOH), which is generated through a self-reconstruction process.[78] However, the NiOOH can easily undergo hydrogenation due to the instability of the Ni^{3+}. To address this challenge, Cai *et al.* synthesized NiOOH/(LDH/α-FeOOH), which contains stabilized NiOOH from introducing α-FeOOH into NiFe-LDH.[79] Density functional theory (DFT) calculations were performed to compare the hydrogenation formation energy (E_H) of the oxygen site in NiOOH and α-FeOOH/NiOOH using a composite model of α-FeOOH/NiOOH (Fig. 3e). The rightmost columns in Fig. 3f indicate the average E_H value of oxygen sites. In the case of NiOOH, the average E_H value was −3.18 eV, whereas it was −2.92 eV for α-FeOOH/NiOOH. A lower E_H indicates a higher tendency for the reduction of Ni^{3+} to Ni^{2+}. The electrochemical measurements demonstrated the highest performance for UOR in a 1 M KOH solution with 0.33 M urea (Fig. 3g). The NiOOH/(LDH/α-FeOOH) required 1.35, 1.37, and 1.40 V *vs.* RHE to reach current densities of 10, 50, and 100 mA cm^{-2}, respectively. Fig. 3h shows the measured double-layer capacitance (C_{dl}) value for the catalysts. The C_{dl} values were 1.6, 2.5, 4.4, and 10.0 mF c^{-2} for LDH, LDH/α-FeOOH, NiOOH/LDH, and NiOOH/(LDH/α-FeOOH), respectively, indicating that NiOOH/(LDH/α-FeOOH) has a large electrochemically active surface area (ECSA).

Huo *et al.* synthesized high-valence metal (V, Mn, Mo) doped FeNi LDH with hollow morphology using spindle-like Fe-MIL-88A.[80] The large atomic radii of high-valence metals result in lattice expansion, which alters the electronic structure. Furthermore, the hollow structure enhances mass and heat transport ability. Among the high-valence metals, the Mo–FeNi LDH exhibited the highest activity for UOR in a 1 M KOH solution with 0.33 M urea. The Mo-FeNi LDH catalyst required only 1.32 V *vs.* RHE, which is 172 mV lower than that of the OER (Fig. 3i). Additionally, Fig. 3j shows the difference between HER||OER, and HER||UOR using a Pt/C||Mo–FeNi LDH two-electrode electrolyzer. While conventional water electrolysis requires 1.49 V *vs.* RHE at 10 mA cm^{-2}, the urea-assisted water electrolysis requires 1.38 V *vs.* RHE, indicating that hydrogen generation occurs at a much lower potential. The DFT calculations demonstrate that Mo doping stabilizes CO* and NH* intermediates during the UOR, leading to a decrease in the energy barrier of the rate-determining step (RDS). More specifically, while the dissociation of adsorbed urea to CO* and NH* requires only 0.12 eV for Mo–FeNi LDH, the FeNi-LDH requires 3.48 eV. This result indicates that the Mo–FeNi LDH exhibits a significantly higher ability to stabilize intermediates (CO*, NH*) than FeNi-LDH. This is because the electron transfer from Ni to Mo, derived from the electronegativity difference, regulates the electronic structure (Fig. 3k and l).

UOR not only decreases the potential required for hydrogen generation but also offers environmental advantages. Thus, 2D structure-based catalysts are being actively researched due to their outstanding catalytic properties. For instance, the $MoSe_2$/$NiSe_2$ exhibits enhanced UOR activity by introducing a heterostructure on TMDs. Additionally, high-valence metal-doped LDH or α-FeOOH, introduced LDH, has shown high performance for UOR. These studies demonstrate the improved performance of 2D structures and suggest infinite possibilities for their application.

3 2D catalysts for hydrazine oxidation

HzOR is highly attractive as an alternative anode reaction for hydrogen generation due to its exceptionally low potential of −0.33 V *vs.* RHE.[81] Furthermore, HzOR produces only N_2 and H_2, which are non-toxic, and since industrial wastewater contains hydrazine, HzOR is even more environmentally friendly. However, noble metals such as Pt and Ru are almost inevitable for high performance in HzOR.[82,83] Therefore, research on catalyst synthesis for HzOR using 2D structures to reduce the use of noble metals is actively being conducted due to their exceptional properties.

Currently, various methods exist for producing 2D materials. However, most of them face challenges in regulating the thickness of nanosheets.[84] Si *et al.* synthesized ∼3 nm-thick few-layer NbS_2 nanosheets from bulk NbS_2 *via* the electrochemical exfoliation method.[85] As shown in Fig. 4a, the single-layered NbS_2 forms a multi-layered structure stacked by van der Waals forces, a common phenomenon in other transition metal dichalcogenides (TMDs). Fig. 4b shows the transmission electron microscopy (TEM) image of synthesized NbS_2 nanosheets. Electrochemical measurements were conducted in 1.0 M KOH with and without 0.5 M hydrazine solution. The LSV curve (Fig. 4c) demonstrates that the HzOR starts at a much lower potential than the Oxygen evolution reaction (OER). Additionally, the bifunctional catalytic activity was evaluated using a two-electrode electrolyzer, employing few-layer NbS_2 nanosheets/CP as a bifunctional electrode for HER and HzOR (Fig. 4d). Fig. 4d shows that the few-layer NbS_2

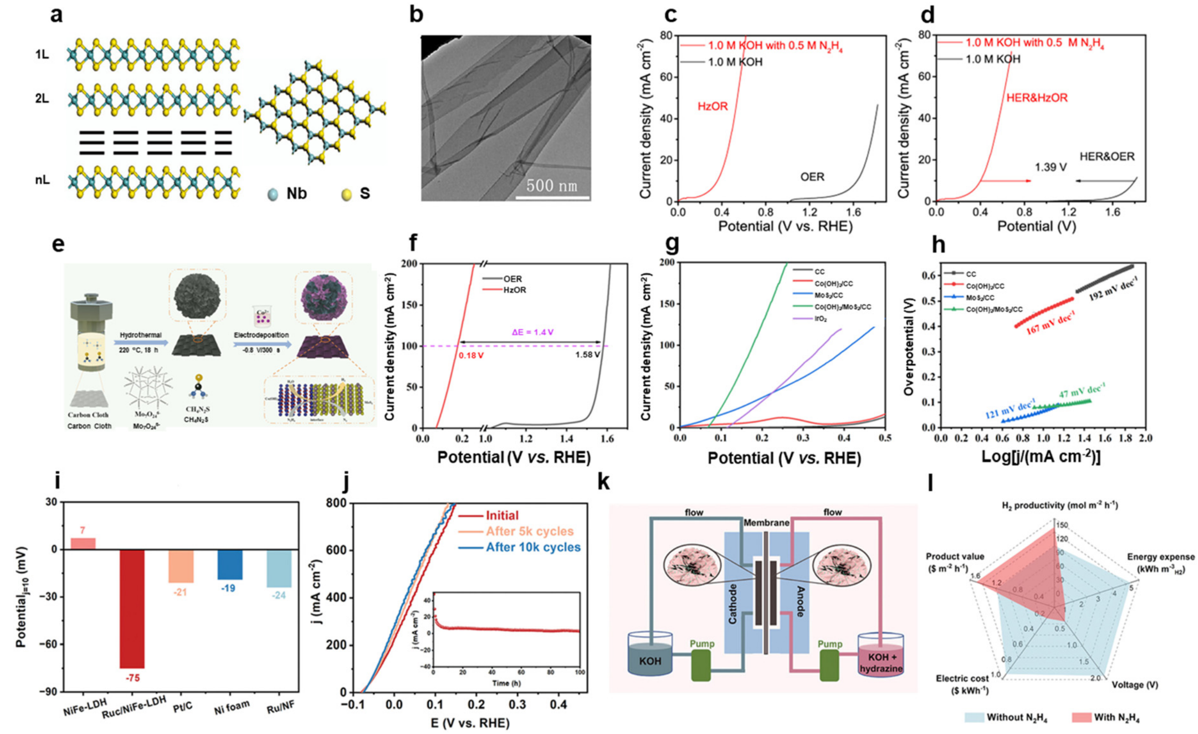

Fig. 4 Various 2D catalysts for the hydrazine oxidation reaction. (a) Structural model of NbS_2, (b) TEM image of a few-layer NbS_2 nanosheet, (c) LSV curve of a few-layer NbS_2 nanosheet for HzOR and OER, and (d) LSV curves of few-layer NbS_2 comparing HzOR||HER and OER||HER performance, reprinted with permission from ref. 85, copyright 2019 American Chemical Society; (e) $Co(OH)_2$/MoS_2 synthesis scheme, (f) LSV curve of $Co(OH)_2$/MoS_2 for HzOR and OER, (g) LSV curve of CC, $Co(OH)_2$/CC, MoS_2/CC, $Co(OH)_2$/MoS_2/CC, and IrO_2 for HzOR, (h) Tafel slope value of CC, $Co(OH)_2$/CC, MoS_2/CC, and $Co(OH)_2$/MoS_2/CC, reprinted with permission from ref. 86, copyright 2023 American Chemical Society; (i) required overpotential to reach 10 mV cm^{-2}, (j) LSV curves after 5 k, 10 k CV cycles and chronoamperometry test, (k) structural model of a two-electrode flow cell, and (l) comparison of efficiency for hydrogen generation with and without hydrazine, reprinted with permission from ref. 87, copyright 2024 Wiley-VCH GmbH.

nanosheets without 0.5 M hydrazine require about 1.7 V *vs.* RHE to deliver 10 mA cm^{-2}. However, with 0.5 M hydrazine, it requires only about 0.4 V *vs.* RHE to produce 10 mA cm^{-2}.

Cheng *et al.* reported $Co(OH)_2/MoS_2$ heterostructure electrocatalysts for HzOR, synthesized *via* hydrothermal and electrodeposition methods.[86] The synthesis process is shown in Fig. 4e. First, MoS_2 nanosheets were synthesized on the carbon cloth (CC) *via* a hydrothermal method. Then, the $Co(OH)_2$ nanosheets were introduced onto MoS_2/CC *via* the electrodeposition method, referred to as $Co(OH)_2/MoS_2$/CC. Fig. 4f indicates the comparative LSV curves for OER and HzOR. $Co(OH)_2/MoS_2$/CC exhibits high catalytic performance for HzOR. To be specific, $Co(OH)_2/MoS_2$/CC requires 1.58 V *vs.* RHE for OER, whereas only 0.18 V *vs.* RHE for HzOR is needed to deliver 100 mA cm^{-2}, resulting in a voltage reduction of 1.4 V *vs.* RHE. The oxidation peak at about 1.1 V *vs.* RHE originated from the oxidation of Co^{2+} to Co^{3+}. Additionally, $Co(OH)_2/MoS_2$/CC exhibits higher performance in HzOR than other samples, including commercial IrO_2 (Fig. 4g). At 0.25 V *vs.* RHE, the current density reached 190 mA cm^{-2}, which is 3.9, 15.6 times higher than MoS_2/CC and $Co(OH)_2$/CC, respectively. The Tafel slopes were calculated for $Co(OH)_2/MoS_2$/CC, $Co(OH)_2$/CC, and MoS_2/CC, revealing values of 47 mV dec^{-1}, 167 mV dec^{-1}, and 121 mV dec^{-1}, respectively. The low Tafel slope of $Co(OH)_2/MoS_2$/CC indicates faster reaction kinetics due to the formation of the heterostructure with 2D material.

Zhu *et al.* synthesized a bifunctional catalyst Ru_c/NiFe-LDH by anchoring a Ru cluster on 2D-structured NiFe LDH through the formation of a Ru–O–Ni/Fe bridge.[87] The Ru–O–Ni/Fe bridge induces a widening of the d-band width in the Ru cluster. As the d-band width widens, the d-band center of the Ru cluster shifts downward. Consequently, more electrons occupy the antibonding molecular orbitals, which weakens the strong adsorption of hydrazine on the Ru surface. The weakened adsorption facilitates enhanced desorption, allowing an effective adsorption–desorption process. The electrochemical measurements are shown in Fig. 4i. While Ru_c/NiFe-LDH required only 75 mV *vs.* RHE to reach 10 mA cm^{-2}, NiFe-LDH, Pt/C, Ni foam, and Ru/NF required 7, −21, −19, and −24 mV *vs.* RHE in 1 M KOH with 0.3 M hydrazine solution, respectively. This result indicates that the Ru_c/NiFe-LDH exhibits superior HzOR activity compared to the other catalysts. The LSV was conducted on Ru_c/NiFe-LDH after 5 k and 10 k cyclic voltammetry (CV) cycles (Fig. 4j). There were no apparent differences between before and after CV cycles, indicating the high stability of the catalyst. Additionally, Ru_c/NiFe-LDH demonstrated high stability for a 100 h chronoamperometry (CA) test at a current density of 10 mA cm^{-2} (Fig. 4j, inset). Furthermore, to evaluate the possibility of industrial usage, the electrochemical measurements were conducted on Ru_c/NiFe-LDH using a two-electrode flow cell (Fig. 4k). Fig. 4l shows the comparison of economic efficiency for hydrogen generation between water electrolysis and hydrazine-assisted water electrolysis. The hydrazine-assisted water electrolysis exhibited higher H_2 productivity (mol m^{-3} h^{-1}) than water splitting and even lower energy expense (kWh $m_{H_2}^{-3}$), leading to a high product value (\$ m^{-2} h^{-1}) and low electric cost (\$ kWh^{-1}).

HzOR has high potential as an alternative OER due to its exceptionally low onset potential. In particular, various 2D structure-based catalysts for HzOR have been reported, demonstrating excellent activity. For example, NbS_2 nanosheets synthesized *via* electrochemical exfoliation, the $Co(OH)_2/MoS_2$ heterostructure catalyst exhibiting fast reaction kinetics, and Ruc/NiFe-LDH, in which the Ru cluster is anchored on the NiFe-LDH. These catalysts have all shown high performance not only for HzOR but also for HER, indicating their potential as bifunctional catalysts. Therefore, these advancements in 2D material-based catalysts contribute to achieving highly efficient hydrogen production.

4 2D catalysts for alcohol oxidation (methanol & ethanol)

The alcohol oxidation reactions, particularly MOR and EOR, have emerged as attractive alternatives to the OER in water electrolysis. Alcohol-assisted water electrolysis not only significantly reduces the overall energy input due to the lower oxidation potentials of alcohols, but also enables the co-generation of value-added chemicals such as formate and acetate.[88] These benefits make MOR and EOR promising anodic reactions for the development of next-generation electrochemical hydrogen production platforms. In addition to their role in assisted water electrolysis, MOR and EOR have also been widely applied in direct alcohol fuel cells (DAFCs), which are regarded as efficient and portable power sources.[89] DAFCs offer several advantages, including high energy density, easy fuel handling, and low operating temperatures.[90] However, MOR suffers from severe catalyst poisoning by CO intermediates, which limits the long-term activity of the electrocatalyst.[91] Meanwhile, EOR involves a more complex reaction pathway, leading to incomplete oxidation and the formation of by-products such as acetaldehyde and acetic acid.[92] To address these challenges, 2D electrocatalysts have been widely explored that can enhance the activity, selectivity, and durability of alcohol oxidation reactions.

Nickel-based catalysts are the most widely explored among transition metals for MOR. Zhu *et al.* synthesized NiMn and NiFe-LDHs uniformly on nickel foam (NF) using a hydrothermal synthesis.[93] Inductively coupled plasma-optical emission spectrometer analysis revealed high-Ni compositions, with Ni/Mn and Ni/Fe atomic ratios of 4.4 and 4.6, respectively. MOR performance of NiMn and NiFe-LDHs was evaluated in 1 M KOH with 3 M methanol solution (Fig. 5a). NiMn-LDH showed superior performance with a lower onset overpotential of 1.30 V *vs.* RHE at 2 mA cm^{-2} than that of NiFe-LDH (1.37 V *vs.* RHE). At the higher current density, NiMn-LDH also showed a smaller working potential of 1.41/1.49 *vs.* RHE at 100/500 mA cm^{-2} compared to NiFe-LDH (1.45/1.62 V *vs.* RHE). The ECSA data showed a significant difference in the catalytic activity of the two catalysts for both MOR and OER (Fig. 5b). NiMn-LDH exhibited three times higher activity than NiFe-LDH for MOR

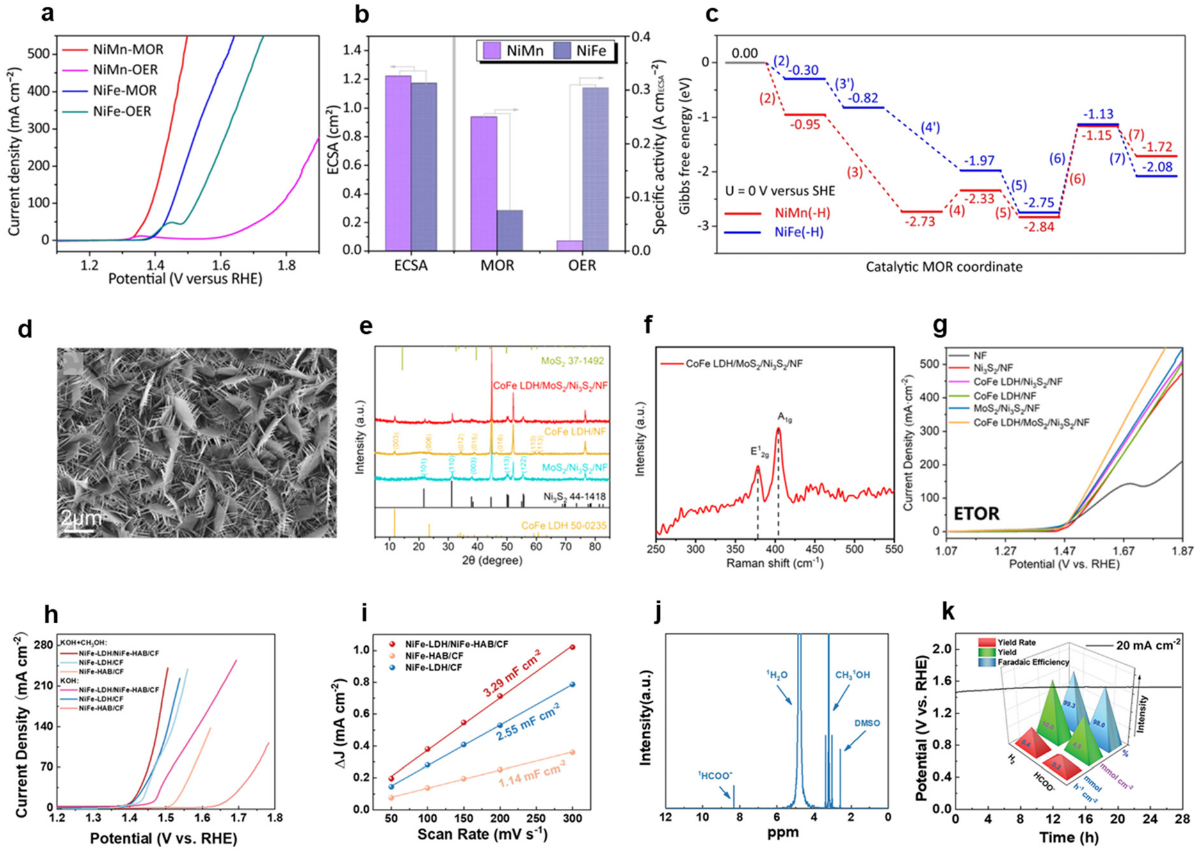

Fig. 5 Various 2D catalysts for alcohol oxidation reaction. (a) LSV curves of NiMn, NiFe LDH for MOR and OER, (b) ECSA value and specific activity for MOR, OER, and (c) DFT calculation of the MOR process, reprinted with permission from ref. 93, copyright 2023 Springer Nature Limited; (d) SEM image of CoFe LDH/MoS_2/Ni_3S_2/NF Astructure, (e) XRD pattern of CoFe LDH/MoS_2/Ni_3S_2/NF structure, (f) Raman spectroscopy of CoFe LDH/MoS_2/Ni_3S_2/NF structure, and (g) comparison of LSV curves for EOR, reprinted with permission from ref. 94, copyright 2024 American Chemical Society; (h) LSV curves of NiFe-LDH/NiFe-HAB/CF and comparison group for OER and MOR, (i) C_{dl} values of NiFe-LDH/NiFe-HAB/CF, NiFe-HABCF, and NiFe-LDH/CF, (j) 1H NMR spectrum of the electrolyte after electrolysis for 1 h at 60 mA cm^{-2} in 1.0 m KOH + 3.0 m CH_3OH solution, and (k) stability test and yield rate, yield, and Faradaic efficiency for HCOO- and H_2, reprinted with permission from ref. 95, 2023 Wiley-VCH GmbH.

but showed sixteen times lower activity for OER. These LSV and ECSA results indicate that NiMn-LDH is more feasible for MOR compared to NiFe-LDH. This difference was elucidated through mechanistic investigations based on density functional theory (DFT) calculations (Fig. 5c). In the case of NiMn-LDH, the MOR pathway consists of a series of exothermic steps that are thermodynamically favorable, including methanol adsorption (reaction (2)), the initial dehydrogenation step (reaction (3)), and formate formation (reaction (5)), which facilitate a rapid and stable reaction process at the early stages. In contrast, the major thermodynamic limitation arises from the formation of $*OCH_2$ in reaction (4), identified as the potential-determining step (PDS). These findings highlight the intrinsic advantages of NiMn-LDH in promoting efficient and active MOR kinetics, providing a reasonable explanation for the superior MOR performance of NiMn-LDH compared to NiFe-LDH.

Li *et al.* developed a heterojunction structure composed of CoFe LDH needles on MoS_2/Ni_3S_2/NF nanoarrays for EOR, which also contains nickel.[94] Although the catalytic performance was assessed for both EOR and UOR, this review will specifically address its application in EOR. The one-dimensional (1D) CoFe LDH needles possess a large surface area and abundant active sites, offering advantages similar to those of 2D materials. CoFe LDH/MoS_2/Ni_3S_2/NF structure incorporates both 2D MoS_2 and 1D CoFe LDH, contributing to a large surface area that enhances the overall electrocatalytic performance, as evidenced by the SEM image (Fig. 5d). In contrast to CoFe LDH and Ni_3S_2, no peaks of MoS_2 were observed in the XRD patterns, which is presumably due to a low loading amount or poor crystallinity (Fig. 5e). In this case, the presence of MoS_2 can be confirmed through other characterization techniques such as Raman spectroscopy or XPS. The Raman spectrum exhibits two strong characteristic peaks at 378 and 404 cm^{-1}, corresponding to the E_2g_1 and A_1g modes, respectively, assigned to MoS_2, thereby confirming its presence (Fig. 5f). In 1 M KOH with 0.34 M ethanol solution, CoFe LDH/MoS_2/Ni_3S_2/NF exhibits the best performance for EOR among those catalysts showing the lowest potential of 1.484 V *vs.* RHE at 50 mA cm^{-2} (Fig. 5g). These results suggest that catalysts combining 1D and 2D structures can exhibit excellent performance in alcohol oxidation.

NiFe-LDH is considered a highly effective OER catalyst due to its layered structure and high catalytic activity.[49] Therefore, when performing methanol electrooxidation to formic acid (MEtF), a type of MOR, using NiFe-LDH, the OER tends to dominate over MEtF within the potential range where OER typically occurs, leading to reduced MEtF activity. Thus, strategies to suppress OER are required. Jiang *et al.* synthesized NiFe-LDH as both a template and precursor for the growth of NiFe hexylaminobenzene (NiFe-HAB) coordination polymers (CPs) on carbon fibers (CFs), referred to as NiFe-LDH/NiFe-HAB/CF, which also contains Ni.[95] By incorporating NiFe-HAB, the OER activity of NiFe-LDH is significantly passivated, thereby enhancing the methanol-to-formate conversion on NiFe-LDH/NiFe-HAB/CF. The LSV results in 1 M KOH solution revealed that the OER activity decreases in the order of NiFe-LDH/CF > NiFe-LDH/NiFe-HAB/CF > NiFe-HAB/CF (Fig. 5h). In contrast, MEtF performance measured in 1 M KOH with 3 M methanol solution demonstrated that NiFe-LDH/NiFe-HAB/CF outperforms the others, with NiFe-LDH/CF showing the next highest activity. NiFe-LDH/NiFe-HAB/CF exhibited a notable potential drop upon the addition of methanol. NiFe-LDH/NiFe-HAB/CF also showed a greater C_{dl} (3.29 mF cm^{-2}) than that of NiFe-LDH (2.55 mF cm^{-2}), indicating superior surface activity (Fig. 5i). After MOR at 60 mA cm^{-2} for 1 h, nuclear magnetic resonance (NMR) analysis revealed that formate is the only oxidation product of methanol on the NiFe-LDH/NiFe-HAB/CF electrode (Fig. 5j). This indicates the high selectivity of the catalyst toward the methanol-to-formate conversion. The chronopotentiometry measurement was conducted at 20 mA cm^{-2} for 28 h (Fig. 5k). During the experiment, value-added formate and hydrogen were co-produced at yield rates of 0.2 and 0.4 mmol h^{-1} cm^{-2} with Faradaic efficiencies of 98.0% and 99.3%, respectively, closely matching the theoretical formate : hydrogen = 1 : 2 molar ratio. In conclusion, the inherently layered nature of NiFe-LDH and the planar structure of the NiFe-HAB CPs categorize NiFe-LDH/NiFe-HAB/CF as a 2D electrocatalyst with extended surface area and abundant active sites, which is considered to contribute to its excellent performance in MEtF.

5 2D catalysts for other organic oxidation

Assisted water electrolysis has been applied not only to alcohols but also to other organic compounds, including glycerol and formic acid.[96,97] Glycerol is a byproduct of biofuel production, and its oxidation in assisted water electrolysis has been studied for the production of valuable chemicals such as formic acid. The selectivity of these oxidation reactions is crucial for producing the desired target products. Additionally, formic acid has been explored as a feedstock for assisted water electrolysis due to its lower theoretical potentials compared to those of the OER. Recently, 2D materials have emerged as promising catalysts in these fields due to their intrinsic physicochemical properties, offering new opportunities for the oxidation of such organic compounds.

Huang *et al.* synthesized a series of 2D conjugated metal–organic frameworks (c-MOFs), denoted as $M_2[NiPcX_8]$, through a solvothermal process. $Co_2[NiPcS_8]$ was developed as a representative catalyst for the GOR.[98] By systematically varying both the metal cations (M = Co, Ni, Cu) and the ligands (X = S, O, NH), the authors evaluated the influence of electronic structure on GOR performance (Fig. 6a). The PXRD pattern of $Co_2[NiPcS_8]$ showed characteristic peaks at $2\theta = 5.0°$, 9.9°, 14.5°, and 25.7°, corresponding to the (100), (200), (300), and (002) lattice planes, respectively (Fig. 6b). These results matched well with DFT-simulated XRD patterns, suggesting an in-plane lattice constant of ~1.8 nm and an interlayer spacing of ~0.35 nm. Electrochemical measurements revealed that $Co_2[NiPcS_8]$ exhibited the highest GOR activity among the $M_2[NiPcS_8]$ catalysts, with the lowest onset potential of 1.2 V *vs.* RHE (Fig. 6c). Furthermore, comparison among $Co_2[NiPcX_8]$ catalysts (X = S, O, NH) demonstrated that $Co_2[NiPcS_8]$ also delivered superior performance at 10 mA cm^{-2} (1.35 V *vs.* RHE), outperforming $Co_2[NiPcO_8]$ (1.44 V) and $Co_2[NiPc(NH)_8]$ (1.51 V) (Fig. 6d). These experimental trends were further supported by DFT calculations, which indicated that the free energy barrier for the rate-determining step in GOR was lowest for $Co_2[NiPcS_8]$ (0.93 eV), compared to 1.00 eV and 1.07 eV for $Co_2[NiPcO_8]$ and $Co_2[NiPc(NH)_8]$, respectively. These findings highlight the crucial role of ligand chemistry and metal–ligand interactions in determining the electrocatalytic activity of 2D c-MOFs.

Yu *et al.* developed a bifunctional electrocatalyst by anchoring Pt single atoms (Pt_{SA}) onto NiCo layered double hydroxides (NiCo LDHs), forming Pt_{SA}–NiCo LDHs.[99] The catalyst was synthesized *via* an electrodeposition process, in which oxygen vacancies within the 2D LDH matrix stabilized the Pt atoms. HAADF-STEM images revealed uniformly distributed bright dots, corresponding to dispersed Pt SAs (Fig. 6e). As shown in Fig. 6f, Pt_{SA}–NiCo LDHs exhibited excellent GOR activity, requiring only 1.298 V *vs.* RHE to reach 100 mA cm^{-2}, significantly lower than the potential for OER (1.568 V). Additionally, at 1.375 V *vs.* RHE, the catalyst achieved 85% glycerol conversion with a high Faradaic efficiency of 88.7% for formate production (Fig. 6g). Based on product analysis *via* NMR, a proposed reaction pathway for glycerol-to-formate conversion involved sequential oxidation steps (Fig. 6h).

Zeng *et al.* developed a PdCu bimetallene featuring abundant crystalline/amorphous (c/a) interfaces and boron doping (B–PdCu-c/a), introduced *via* a solvothermal process with $NaBH_4$ post-treatment.[100] The incorporation of the p-block element boron induced d–sp (d–p) orbital hybridization with Pd-based metals, effectively modulating the electronic structure and enhancing the catalytic activity toward the FAOR. The XRD patterns (Fig. 6i) revealed that, following $NaBH_4$ treatment, the diffraction peaks of B–PdCu-c/a shifted to lower 2θ angles, indicative of lattice expansion due to boron incorporation into the PdCu matrix. Electrochemical measurements under FAOR||HER and OER||HER configurations demonstrated the superior performance of the B–PdCu-c/a catalyst. As shown in Fig. 6j, the cell voltage at 10 mA cm^{-2} in the FAOR||HER system

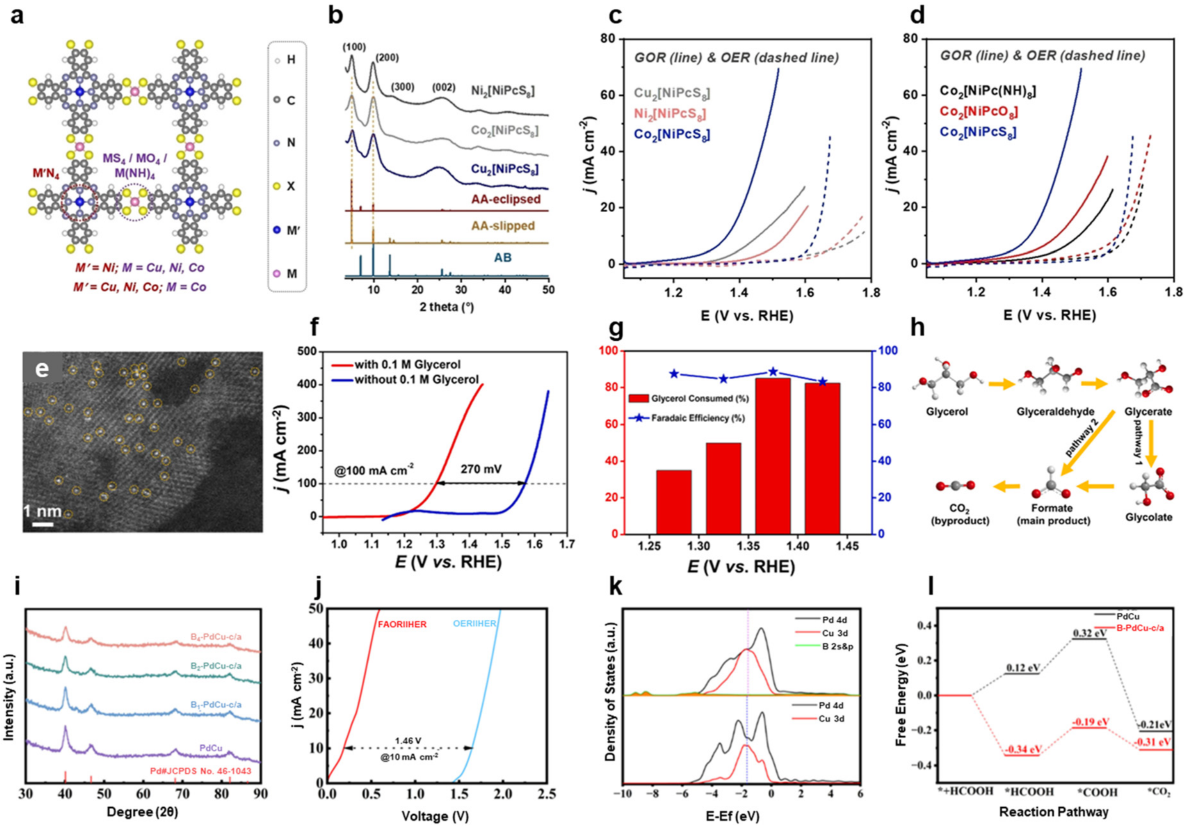

Fig. 6 Various 2D catalysts for other organic oxidation reactions. (a) Structural model of $M_2[M'PcX_8]$, (b) XRD patterns of experimental and simulated catalysts, LSV curves of (c) $M_2[NiPcS_8]$ (M = Cu, Ni, Co) and (d) $Co_2[NiPcX_8]$ (X = S, O, NH) during the GOR, reprinted with permission from ref. 98, copyright 2024 Wiley-VCH GmbH; (e) HAADF-STEM image of Pt_{SA}–NiCo LDH, (f) LSV curves of Pt_{SA}–NiCo LDH for OER and GOR, (g) Faradaic efficiency of glycerol-to-formic acid conversion at different applied potentials, and (h) the oxidation process of glycerol, reprinted with permission from ref. 9, copyright 2023 Elsevier; (i) XRD patterns of B–PdCu-c/a bimetallene catalysts, (j) LSV curves comparing FAOR||HER and OER||HER performance, (k) calculated density of states of B–PdCu-c/a bimetallene, and (l) the free-energy pathway for the FAOR, reprinted with permission from ref. 100, copyright 2024 American Chemical Society.

was significantly reduced to 0.19 V, in contrast to 1.65 V under conventional OER||HER conditions. DFT calculations revealed that B doping promotes strong d–sp orbital hybridization, resulting in the upward shift of the d-band center and enhanced intermediate adsorption (Fig. 6k). Furthermore, the free energy pathway analysis (Fig. 6l) indicated that B–PdCu-c/a possesses a lower energy barrier (0.15 eV) for the C–H bond cleavage step, the rate-determining step in FAOR, compared to PdCu (0.20 eV), thereby facilitating improved catalytic kinetics.

Various 2D electrocatalysts have demonstrated significant potential for assisted water electrolysis, extending beyond the oxidation of alcohols to include glycerol and formic acid. The studies discussed various strategies to enhance catalytic activity and selectivity, such as metal–ligand modulation in 2D c-MOFs, the incorporation of atomically dispersed noble metals on LDH supports, and electronic structure engineering through dopant-induced orbital hybridization. These approaches reduce the anodic potential compared to the traditional OER. Furthermore, in the case of GOR, they enable the synthesis of value-added products. These developments highlight the promise of 2D catalysts as efficient and tunable materials for electrochemical energy conversion systems.

6 Industrial implementation of assisted water electrolysis

To bridge laboratory-scale research with practical deployment, it is important to consider the cell and reactor configurations employed for industrial hydrogen generation. Among these, the zero-gap electrolyzer system has been most widely adopted, particularly under alkaline or anion-exchange conditions. A typical zero-gap configuration consists of stacked anode and cathode plates (current collectors), gaskets, porous transport layers (PTLs), electrocatalysts, an anion-exchange membrane (AEM), and an electrolyte circulation system such as an integrated peristaltic pump (Fig. 7a and d).[129,130] Compared to conventional three-electrode configurations such as H-type or one-pot cells, zero gap two-electrode systems offer distinct advantages for scale-up, including a large effective reaction area, reduced ohmic resistance, and improved energy efficiency.

Recent studies have demonstrated that assisted water electrolysis can be successfully integrated into zero-gap electrolyzers. For example, Yang *et al.* studied AEMWE performance for UOR using NiO/Co_3O_4 as anode and NiCoP

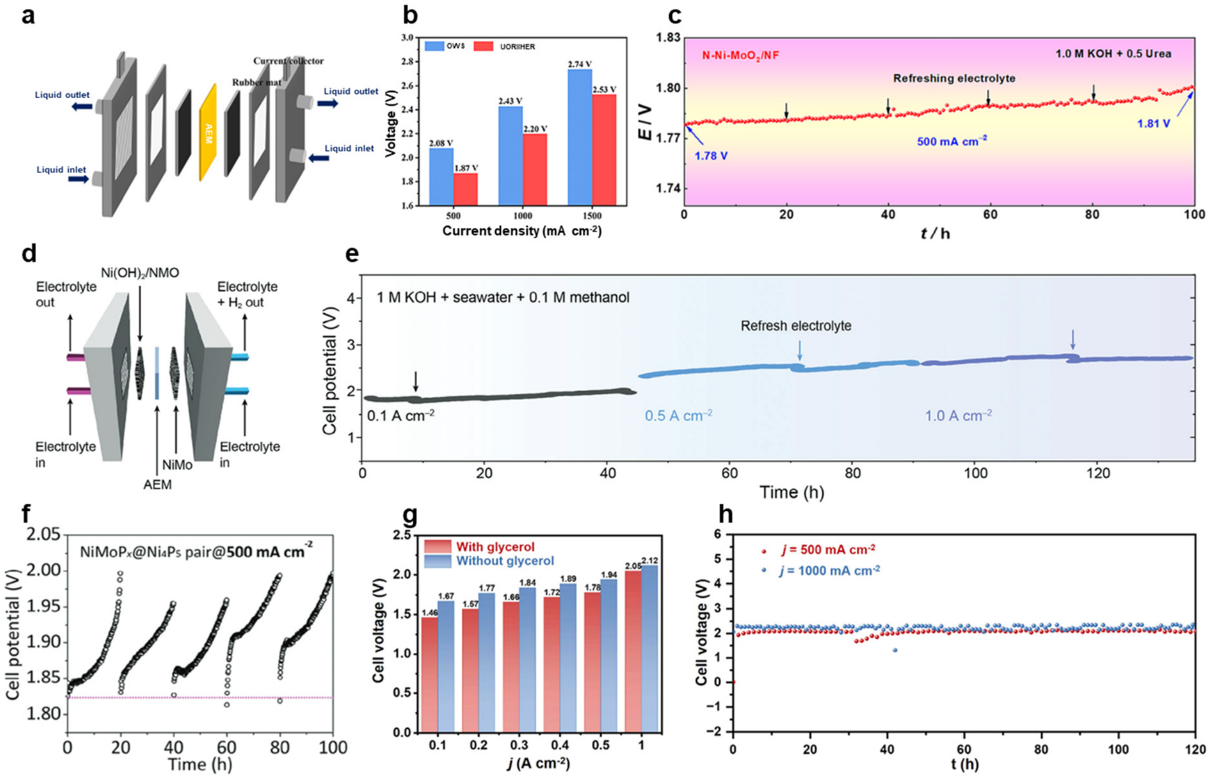

Fig. 7 Industrial H_2 production using alternative anodic reactions. (a) Schematic of the cell configuration, and (b) Overpotentials of NiO/Co_3O_4||NiCoP AEMWE with and without urea under high-current conditions, reprinted with permission from ref. 129, copyright 2025 Springer Nature; (c) stability test of N–Ni–MoO_2/NF catalysts at 500 mA cm^{-2} for 100 h, reprinted with permission from ref. 131, copyright 2023 Elsevier; (d) schematic of the cell configuration, and (e) stability test of $Ni(OH)_2$/NMO catalyst with 0.1 M methanol for over 130 h at high current densities, reprinted with permission from ref. 130, copyright 2024 Wiley-VCH GmbH; (f) stability test of $NiMoP_x@Ni_4P_5$ pair catalyst at 500 mA cm^{-2} for 100 h, reprinted with permission from ref. 132, copyright 2024 Wiley-VCH GmbH; (g) Overpotentials of CoFe hydroxide catalysts with and without 0.5 M glycerol under high-current conditions, and (h) stability tests of CoFe hydroxide catalyst at 500 and 1000 mA cm^{-2} for 120 h, reprinted with permission from ref. 133, copyright 2025 Elsevier.

as the cathode.[129] The UOR||HER system achieved energy savings of 210, 230, and 210 mV compared with overall water splitting at 500, 1000, and 1500 mA cm^{-2}, respectively (Fig. 7b). In addition, Qian *et al.* investigated N–Ni–MoO_2/NF catalysts, which exhibited stable operation ($V_{\text{initial}}/V_{\text{final}}$ = 98.3%) at 500 mA cm^{-2} for 100 h in the presence of urea, with the electrolyte refreshed every 20 h (Fig. 7c).[131] Similarly, $Ni(OH)_2$/NMO catalysts coupled with 0.1 M methanol achieve stable operation for over 130 h at high current densities (Fig. 7e).[130] $NiMoP_x@Ni_4P_5$ pairs sustain 500 mA cm^{-2} for 100 h under 6.0 M KOH and 1.0 M CH_3OH at 65 °C, with electrolyte refreshed every 20 h (Fig. 7f).[132] Moreover, CoFe hydroxide catalysts not only exhibit significantly reduced overpotentials when operated with glycerol (Fig. 7g) but also maintain stability at 500 and 1000 mA cm^{-2} for 120 h (Fig. 7h).[133] Collectively, these demonstrations highlight the scalability and durability of 2D catalyst-based assisted electrolysis under industrially relevant conditions.

Nevertheless, further challenges remain in reactor design (*e.g.*, flow-field optimization, gas–liquid management), long-term electrode stability under fluctuating loads, and techno-economic viability considering feedstock availability and by-product valorization. Importantly, unlike conventional OER, assisted water electrolysis inherently relies on the continuous supply of organic or nitrogenous feedstocks. Therefore, evaluation at the industrial scale must necessarily include feedstock delivery and management processes, such as reactant feeding strategies, concentration control, and by-product separation. Without such considerations, performance metrics cannot be directly extrapolated to practical hydrogen generation.

7 Summary and outlook

Assisted water electrolysis has emerged as a promising strategy for not only reducing the energy demand of hydrogen production but also enabling the co-generation of valuable chemicals and the remediation of environmental pollutants. A wide range of alternative oxidation reactions, including HzOR, UOR, MOR, EOR, GOR, and FAOR, have been extensively studied in combination with diverse catalytic systems to enhance overall electrolysis efficiency.

In particular, 2D materials such as LDHs, TMDs, MXenes, metallenes, and graphene-based materials have received considerable attention owing to their high surface area, electrical conductivity, and tunable catalytic activity. This review provides a comprehensive overview of recent developments in 2D-based catalysts for various assisted anodic reactions in water electrolysis. Table 2 provides specific electrochemical performance values such as the Tafel slope, potential (at 10, 50, and 100 mA cm^{-2}), and long-term stability. Each parameter plays a major role in evaluating the performance of catalysts. In comparison, Fig. 8 highlights the electrochemical performance of these reactions, showing that HzOR exhibits significantly lower overpotentials than UOR, MOR, and GOR. This indicates that HzOR is a highly favorable anodic alternative from an energy efficiency perspective.

These insights underscore the pivotal role of feedstock selection and 2D catalyst design in enhancing the energy efficiency and practicality of assisted electrolysis systems. Building upon this foundation, several future research directions are proposed to accelerate the development and implementation of 2D-based electrocatalysts in real-world AWE applications:

(1) Various 2D-based materials have been employed as catalyst supports to improve distribution and structural stability for main catalysts, and synergistic effects. However, when used alone, these materials often exhibit limited intrinsic catalytic activity, indicating the need for coupling with additional active catalysts, such as noble metals. To overcome this limitation, high-entropy (HE) strategies have recently gained traction in the field of catalysis. High-entropy alloy (HEA) catalysts, characterized by multiple principal elements, offer four main effects, including the cocktail effect, lattice distortion, sluggish diffusion, and high configurational entropy, that enable tunable electronic structures and improved catalytic behavior.[134,135] In particular, high-entropy transition metal dichalcogenides (HE-TMDs) as 2D catalysts have demonstrated enhanced activity for oxidation reactions without requiring noble metals, owing to their modulated electronic environments.[136–139] This approach is not limited to TMDs, other 2D materials (LDHs, MXenes, and metallenes) can also be tailored using high-entropy designs to optimize electrocatalytic performances.[140,141] Moreover, the inherent thermodynamic stability of high-entropy configurations contributes to improved durability, bringing such materials closer to practical application and commercialization.

(2) It is well-established that edge sites in 2D catalysts exhibit significantly higher catalytic activity than their in-plane counterparts, due to their unsaturated coordination and favorable adsorption properties.[56] While conventional doping strategies have primarily focused on in-plane substitution, edge-site doping is emerging as a promising approach to enhance performance further. Doping at edge sites not only activates additional reaction centers but also offers thermodynamic advantages, as the formation energy of dopants is generally lower at edge sites compared to basal planes.[142] This enhances both the stability and activity of doped atoms, enabling synergistic improvements in overall catalytic performance.

(3) A lot of studies on 2D-based catalysts report high catalytic performance under laboratory conditions, particularly at elevated concentrations of the molecular feedstocks. While one of the key advantages of assisted water electrolysis is the remediation of organic and nitrogen-containing pollutants, the concentrations used in experimental setups often far exceed those found in real wastewater streams.[143,144] To enhance the practical relevance of these studies, electrochemical testing under realistic, low-concentration conditions is essential. In addition, most current research is conducted under strongly acidic or alkaline environments, which are not always compatible with industrial or environmental systems.[24,145–149] Future efforts should focus on catalyst evaluation under neutral or near-neutral pH conditions to better reflect practical application scenarios and long-term operational stability.

(4) Furthermore, in real-world wastewater streams, multiple organic and nitrogen-containing compounds often coexist, presenting a complex chemical environment that differs significantly from simplified laboratory conditions.[150,151] However, most current studies on assisted water electrolysis focus on single-component feedstocks, limiting the applicability of these systems to practical situations.[76,152] Future research should therefore prioritize the development of multi-component oxidation strategies, wherein catalysts are designed to selectively and simultaneously activate different types of molecules. This could involve tandem or cascade oxidation pathways, where intermediates from one oxidation reaction participate in subsequent transformations, potentially enabling the formation of more complex and valuable chemical products. Such approaches would not only improve energy efficiency and pollutant removal under realistic conditions but also expand the functional scope of assisted electrolysis by coupling hydrogen production with advanced molecular synthesis.

2D materials have demonstrated exceptional promise as catalysts for assisted water electrolysis, enabling energy-efficient hydrogen production while simultaneously achieving environmental remediation and the synthesis of value-added chemicals. This review has provided a comprehensive overview of the fundamental principles, representative oxidation reactions, and recent advances in the design of 2D-based catalysts. By bridging the gap between theoretical understanding and practical implementation, these insights contribute to the global goal of sustainable hydrogen technologies and carbon neutrality.

Author contributions

Hyojung Lim: conceptualization, data curation, investigation, methodology, visualization, writing—original draft preparation, writing—review, and editing. Seonghyeon Park: conceptualization, investigation, writing—original draft preparation, writing—review, and editing. Jinuk Choi: conceptualization, investigation, writing—original draft

Table 2 Comparison of 2D-based catalysts for assisted water electrolysis

Reaction	Catalyst	Electrolyte	Potential at 10 mA (V *vs.* RHE)	Potential at 50 mA (V *vs.* RHE)	Potential at 100 mA (V *vs.* RHE)	Tafel slope (mV dec^{-1})	Target products/FE (product)	Stability performance (CV, CA, CP)	Ref.
HzOR	NbS_2	1 M KOH + 0.5 M hydrazine	~0.37	~0.53	—	—	—	10 mA cm^{-2} 10 h	85
	$Co(OH)_2/MoS_2/CC$	1 M KOH + 0.4 M hydrazine	—	—	0.18	11	—	~0.14 V *vs.* RHE 11 h	86
	N–NiZnCu LDH/rGO	1 M KOH + 0.5 M hydrazine	0.014	0.021	0.045	20	—	3000 cycle CV	101
	Ru_c/NiFe-LDH	1 M KOH + 0.3 M hydrazine	−0.075	—	—	40.4	—	10 000 cycle CV	87
	AR-$Co(OH)_2/Ti_3C_2(OH)_x$	1 M KOH + 0.5 M hydrazine	0.995	—	—	56	—	1.15 V *vs.* RHE 50 h	102
	S–CuNiCo-LDH	1 M KOH + 0.02 M hydrazine	~0.29	—	~0.65	73.3	—	0.7 *vs.* RHE 20 h	103
	CC@WS_2/Ru-450	1 M KOH + 0.5 M hydrazine	−0.074	—	—	42.2	—	10 mA cm^{-2} 100 h	104
	NiCo@C/MXene/CF	1 M KOH + 0.5 M hydrazine	−0.096	—	−0.025	73	—	100 mA cm^{-2} 30 h	105
UOR	CoFe LDH/MoS_2/Ni_3S_2/NF	1 M KOH + 0.5 M urea	1.423	—	—	—	—	50 mA cm^{-2} 50 h	94
	N-NiZnCu LDH/rGO	1 M KOH + 0.5 M urea	1.304	1.426	1.467	29	—	3000 cycle CV	101
	FeCuCoNiZn-LDH/CC	1 M KOH + 0.33 M urea	1.326	—	—	120	—	1.53 V *vs.* RHE ~70 h	106
	$Ni_{0.67}Co_{0.33}(OH)_2/CC$	1 M KOH + 0.5 M urea	1.23	—	—	40	—	1.40 V *vs.* RHE 10 h	107
	MoS_4-LDH/NF	1 M KOH + 0.33 M urea	1.34	—	—	29	—	10 mA cm^{-2} 24 h	108
	FQD/CCoNi-LDH/NF	1 M KOH + 0.5 M urea	1.36	—	1.42	17	—	1.40 V *vs.* RHE 15 h	109
	NiS/MoS_2@CC	1 M KOH + 0.5 M urea	1.36	—	1.38	24.2	—	1.36 *vs.* RHE ~27 h	110
	$MoSe_2/NiSe_2$	1 M KOH + 0.5 M urea	1.35	1.41	1.47	68	—	100 mA cm^{-2} 100 h	77
	Mo–FeNi LDH	1 M KOH + 0.33 M urea	1.31	—	—	16.9	—	50 mA cm^{-2} 12 h	80
	MoS_2/Ni_3S_2	1 M KOH + 0.5 M urea	1.44	—	—	—	—	3000 cycle CV	111
	CoS_2–MoS_2	1 M KOH + 0.5 M urea	1.29	—	—	32	—	~1.29 V *vs.* RHE 30 h	112
	NiMoV LDH	1 M KOH + 0.33 M urea	—	—	1.4	24.29	—	1.40 V *vs.* RHE 30 h	113
	NiS_2–MoS_2	1 M KOH + 0.33 M urea	—	—	~1.54	29.9	—	1.6 V *vs.* RHE 10 h	114
	Co_1Mn_1 LDH/NF	1 M KOH + 0.33 M urea	1.326	—	—	73	—	1.326 V *vs.* RHE 10 h	115
	NiS/MoS_2@FCP	1 M KOH + 0.4 M urea	—	1.42	1.43	31	—	1000 cycle CV	116
	NiOOH/(LDH/α-FeOOH)	1 M KOH + 0.33 M urea	1.35	1.37	1.4	30.1	—	—	79

Table 2 *(continued)*

Reaction	Catalyst	Electrolyte	Potential at 10 mA (V *vs.* RHE)	Potential at 50 mA (V *vs.* RHE)	Potential at 100 mA (V *vs.* RHE)	Tafel slope (mV dec^{-1})	Target products/FE (product)	Stability performance (CV, CA, CP)	Ref.
MOR	NiMn-LDHs	1 M KOH + 3 M CH_3OH	1.33	—	1.41	39.4	Formate/97.3	100 mA cm^{-2} 20 h	93
	NiFe-LDH/NiFe-HAB/CF	1 M KOH + 3 M CH_3OH	—	1.44	1.46	—	Formate/98	20 mA cm^{-2} 28 h	95
	$Ni_{0.33}Co_{0.67}(OH)_2$/NF	1 M KOH + 0.5 M CH_3OH	1.33	—	—	17	Formate/~100	1.35 V *vs.* RHE 20 h	117
	NiSe/$MoSe_2$/CC	1 M KOH + 1.0 M CH_3OH	—	—	1.38	14	Formate/–	1.41 V *vs.* RHE 120 h	118
	$NiFe_xP$@NiCo-LDH/CC	1 M KOH + 0.5 M CH_3OH	—	1.42	1.425	—	Formate/~100	0.96 V *vs.* RHE 10 h	119
	NiCo-LDH-E	1 M KOH + 1.0 M CH_3OH	~1.40	—	—	28.7	—	—	120
	$Cu_{0.33}$CoCo-LDH/CF	1 M KOH + 3 M CH_3OH	1.28	—	—	67.8	Formate/99	20 mA cm^{-2} 24 h	121
	Co_xP@NiCo-LDH/NF	1 M KOH + 0.5 M CH_3OH	1.24	1.32	1.34	—	Formate/~100	1.35 V *vs.* RHE 20 h	122
EOR	CoFe LDH/MoS_2/Ni_3S_2/NF	1 M KOH + 0.34 M C_2H_5OH	—	1.484	—	—	—	50 mA cm^{-2} 50 h	94
	Pt/N–$Ti_3C_2T_x$	0.5 M H_2SO_4 + 1.0 M C_2H_5OH	—	—	—	275.92	—	—	123
	NiAl-LDH-NSs	1 M NaOH + 1.0 M C_2H_5OH	~1.444	—	—	—	—	—	124
	NiCo-LDH-E	1 M KOH + 1.0 M C_2H_5OH	~1.40	—	—	50.13	—	—	120
	U-NiFe LDH	1 M KOH + 1.0 M C_2H_5OH	1.344	—	—	32.7	—	100 mA cm^{-2} 10 h	125
	$PtSe_2$	0.1 M KOH + 0.5 M C_2H_5OH	~0.58	—	—	177	—	—	126
	Pd/DB-Ti_3C_2	1 M KOH + 1.0 M C_2H_5OH	~0.51	—	—	158	—	2000 cycle CV	127
GOR	$Co_2[NiPcS_8]$	1 M KOH + 0.1 M glycerol	1.35	—	—	102	Formate/>85	10 mA cm^{-2} 12 h	98
	Pt_{SA}–NiCo LDH/NF	1 M KOH + 0.1 M glycerol	—	—	1.298	68.6	Formate/88.7	—	99
	NiVRu-LDHs NAs/NF	1 M KOH + 0.1 M glycerol	1.24	1.3	1.33	40.7	Formate/97	1.40 V *vs.* RHE 10 h	96
FAOR	$PtTe_2$ NSs/C	0.5 M H_2SO_4 + 0.5 M formic acid	~0.3	—	—	208	—	—	97
	Pd/$Ti_3C_2T_x$-rGO	0.5 M H_2SO_4 + 0.5 M formic acid	~0.311	—	—	—	—	—	128

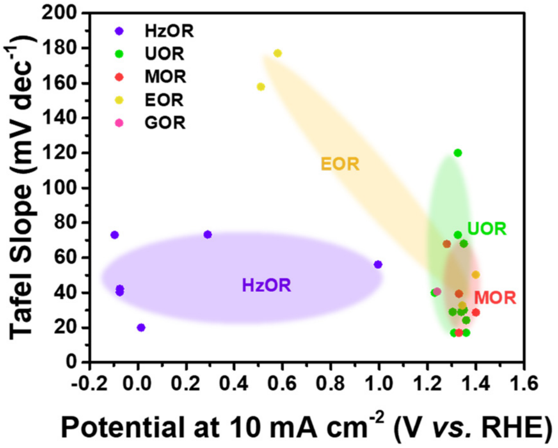

Fig. 8 Comparative analysis of electrochemical performance in assisted water electrolysis systems utilizing various molecular feedstocks.

preparation, writing—review, and editing. Junho Shim: resources, visualization, writing—review, and editing. Subramani Surendran: supervision, validation, visualization, writing—review, and editing. Uk Sim: conceptualization, investigation, visualization, supervision, funding acquisition, validation, writing—original draft preparation, writing—review, and editing.

Conflicts of interest

There are no conflicts to declare.

Data availability

No primary research results, software, or code have been included, and no new data were generated or analysed as part of this review.

Acknowledgements

This work was supported by the Korea Institute of Energy Technology Evaluation and Planning (KETEP) and the Ministry of Trade, Industry and Energy (MOTIE) of the Republic of Korea (No. 20224000000320 and No. RS-2025-07852969). This work was also supported by the Korea Institute of Energy Technology Evaluation and Planning (KETEP) grant funded by the Korea government (MOTIE) (No. RS-2024-00421291, Clean Hydrogen and Ammonia Innovation Research Center).

References

1 S. C. Jesudass, S. Surendran, D. J. Moon, S. Shanmugapriya, J. Y. Kim, G. Janani, K. Veeramani, S. Mahadik, I. G. Kim, P. Jung, G. Kwon, K. Jin, J. K. Kim, K. Hong, Y. I. Park, T.-H. Kim, J. Heo and U. Sim, Defect engineered ternary metal spinel-type Ni-Fe-Co oxide as bifunctional electrocatalyst for overall electrochemical water splitting, *J. Colloid Interface Sci.*, 2024, **663**, 566–576.

2 G. Janani, S. Surendran, D.-K. Lee, S. Shanmugapriya, H. Lee, Y. Subramanian and U. Sim, Aggregation induced edge sites actuation of 3D $MoSe_2$/rGO electrocatalyst for high-performing water splitting system, *Aggregate*, 2024, **5**, e430.

3 S. Mahadik, S. Surendran, D. J. Moon, J. Y. Kim, G. Janani, S. C. Jesudass, K. Veeramani, H. Choi, S. Shanmugapriya, I. G. Kim, P. Jung, Y. I. Park, J. Heo, T.-H. Kim, K. Hong and U. Sim, Structurally engineered highly efficient electrocatalytic performance of 3-dimensional Mo/Ni chalcogenides for boosting overall water splitting performance, *Chemosphere*, 2024, **352**, 141233.

4 Y.-H. Wang, L. Li, J. Shi, M.-Y. Xie, J. Nie, G.-F. Huang, B. Li, W. Hu, A. Pan and W.-Q. Huang, Oxygen defect engineering promotes synergy between adsorbate evolution and single lattice oxygen mechanisms of OER in transition metal-based (oxy)hydroxide, *Adv. Sci.*, 2023, **10**, 2303321.

5 K. Zhang and R. Zou, Advanced transition metal-based OER electrocatalysts: Current status, opportunities, and challenges, *Small*, 2021, **17**, 2100129.

6 K. Jin, J. Park, J. Lee, K. D. Yang, G. K. Pradhan, U. Sim, D. Jeong, H. L. Jang, S. Park, D. Kim, N.-E. Sung, S. H. Kim, S. Han and K. T. Nam, Hydrated manganese(II) phosphate ($Mn_3(PO_4)_2·3H_2O$) as a water oxidation catalyst, *J. Am. Chem. Soc.*, 2014, **136**, 7435–7443.

7 G. Janani, S. Surendran, D. J. Moon, P. S. Ramesh, J. Y. Kim, Y. Lim, K. Veeramani, S. Mahadik, S. C. Jesudass, J. Choi, I. G. Kim, P. Jung, H. Choi, G. Kwon, K. Jin, J. K. Kim, Y. I. Park, J. Heo, K. Hong, Y. S. Kang and U. Sim, Ambipolar nature accelerates dual-functionality on Ni/Ni_3-N@NC for simultaneous hydrogen and oxygen evolution in electrochemical water splitting system, *Adv. Sustainable Syst.*, 2024, **8**, 2400059.

8 Y. Lim, S. Surendran, W. So, S. Shanmugapriya, C. Jo, G. Janani, H. Choi, H. S. Han, H. Choi, Y.-H. Yun, T.-H. Kim, M.-J. Kim, K. Jin, J. K. Kim and U. Sim, In situ decorated Cu_2FeSnS_4 nanosheet arrays for low voltage hydrogen production through the ammonia oxidation reaction, *Mater. Chem. Front.*, 2023, **7**, 5843–5857.

9 H. Choi, S. Surendran, D. Kim, Y. Lim, J. Lim, J. Park, J. K. Kim, M.-K. Han and U. Sim, Boosting eco-friendly hydrogen generation by urea-assisted water electrolysis using spinel M_2GeO_4 (M = Fe, Co) as an active electrocatalyst, *Environ. Sci.: Nano*, 2021, **8**, 3110–3121.

10 P. Arora, K. Bhadauriya, L. Singh, A. Goyal, S. Verma, B. Singh and A. Draksharapu, 3d–2p–5d orbital synergy in electrocatalytic hydrazine oxidation assisted water splitting with industrial scale current density, *Inorg. Chem.*, 2025, **64**, 5069–5076.

11 F. Arshad, T. u. Haq, A. Khan, Y. Haik, I. Hussain and F. Sher, Multifunctional porous NiCo bimetallic foams toward water splitting and methanol oxidation-assisted hydrogen production, *Energy Convers. Manage.*, 2022, **254**, 115262.

12 F. Arshad, T.u. Haq, I. Hussain and F. Sher, Recent advances in electrocatalysts toward alcohol-assisted, energy-saving hydrogen production, *ACS Appl. Energy Mater.*, 2021, **4**, 8685–8701.

13 B. Zhu, Z. Liang and R. Zou, Designing advanced catalysts for energy conversion based on urea oxidation reaction, *Small*, 2020, **16**, 1906133.

14 Y. Tian, Z. Mao, L. Wang and J. Liang, Green chemistry: Advanced electrocatalysts and system design for ammonia oxidation, *Small Struct.*, 2023, **4**, 2200266.

15 Q. Qian, J. Zhang, J. Li, Y. Li, X. Jin, Y. Zhu, Y. Liu, Z. Li, A. El-Harairy, C. Xiao, G. Zhang and Y. Xie, Artificial heterointerfaces achieve delicate reaction kinetics towards hydrogen evolution and hydrazine oxidation catalysis, *Angew. Chem., Int. Ed.*, 2021, **133**, 6049–6058.

16 J. Ren, L. Xing, T. Lai and Y. Zhao, Boosting hydrogen production coupling with electrochemical methanol oxidation to formate using monolayered layered double hydroxide nanosheets, *Ind. Eng. Chem. Res.*, 2023, **62**, 17553–17561.

17 G. Wu, X. Dong, J. Mao, G. Li, C. Zhu, S. Li, A. Chen, G. Feng, Y. Song, W. Chen and W. Wei, Anodic glycerol oxidation to formate facilitating cathodic hydrogen evolution with earth-abundant metal oxide catalysts, *Chem. Eng. J.*, 2023, **468**, 143640.

18 C. Jo, S. Surendran, M.-C. Kim, T.-Y. An, Y. Lim, H. Choi, G. Janani, S. Cyril Jesudass, D. Jun Moon, J. Kim, J. Young Kim, C. Hyuck Choi, M. Kim, J. Kyu Kim and U. Sim, Meticulous integration of N and C active sites in Ni_2P electrocatalyst for sustainable ammonia oxidation and efficient hydrogen production, *Chem. Eng. J.*, 2023, **463**, 142314.

19 J. Choi, H. Lim, S. Surendran, X. Lu, K. Jin, H. Park, H.-Y. Jung and U. Sim, Dichalcogenides as emerging electrocatalysts for efficient ammonia synthesis: A focus on mechanisms and theoretical potentials, *Adv. Funct. Mater.*, 2025, **35**, 2422585.

20 R. Zhang, S. Zhang, Y. Guo, C. Li, J. Liu, Z. Huang, Y. Zhao, Y. Li and C. Zhi, A Zn–nitrite battery as an energy-output electrocatalytic system for high-efficiency ammonia synthesis using carbon-doped cobalt oxide nanotubes, *Energy Environ. Sci.*, 2022, **15**, 3024–3032.

21 X. Qiang, Y. Yao, J. Yin, P. Da, Z. Mu, K. Shen, Y. Sun, Y. Zhang, P. Li, Z. Li, P. Xi and C.-H. Yan, Activating La–O–Ni bridge in ordered macroporous interface for electrochemical urea wastewater purification, *Angew. Chem., Int. Ed.*, 2025, **64**, e202424014.

22 V. S. Protsenko, L. S. Bobrova, T. E. Butyrina and O. D. Sukhatskyi, Thermodynamics of electrochemical urea oxidation reaction coupled with cathodic hydrogen evolution reaction in an alkaline solution: Effect of carbonate formation, *Int. J. Hydrogen Energy*, 2024, **59**, 354–358.

23 V. S. Protsenko, Thermodynamic aspects of urea oxidation reaction in the context of hydrogen production by electrolysis, *Int. J. Hydrogen Energy*, 2023, **48**, 24207–24211.

24 A. Song, Y. Wei, X. Jin, Y. Ma, Y. Wang and J. Yang, Decoupled water reduction and hydrazine oxidation by fast proton transport MoO_3 redox mediator for hydrogen production, *Small*, 2025, **21**, 2407783.

25 F. H. Gül, H. A. Deveci, A. Deveci, O. Akyıldırım and M. L. Yola, Hydrazine imprinted electrochemical sensor based on cobalt-barium stannate nanoparticles incorporated-functionalized MWCNTs nanocomposite for hydrazine determination in tap water samples, *Microchim. Acta*, 2025, **192**, 124.

26 J. Shi, Q. Sun, J. Chen, W. Zhu, T. Cheng, M. Ma, Z. Fan, H. Yang, F. Liao, M. Shao and Z. Kang, Nitrogen contained rhodium nanosheet catalysts for efficient hydrazine oxidation reaction, *Appl. Catal., B*, 2024, **343**, 123561.

27 A. B. Anderson and H. A. Asiri, Reversible potentials for steps in methanol and formic acid oxidation to CO_2; adsorption energies of intermediates on the ideal electrocatalyst for methanol oxidation and CO_2 reduction, *Phys. Chem. Chem. Phys.*, 2014, **16**, 10587–10599.

28 M. Singh, H. M. Sharma, J. Kaur, D. K. Das, M. Ubaidullah, R. K. Gupta and A. Kumar, Engineering of electrocatalysts for methanol oxidation reaction: Recent advances and future challenges, *Mol. Catal.*, 2024, **557**, 113982.

29 C. Lamy, B. Guenot, M. Cretin and G. Pourcelly, Kinetics analysis of the electrocatalytic oxidation of methanol inside a DMFC working as a PEM electrolysis cell (PEMEC) to generate clean hydrogen, *Electrochim. Acta*, 2015, **177**, 352–358.

30 Z. H. N. Al-Azri, W.-T. Chen, A. Chan, V. Jovic, T. Ina, H. Idriss and G. I. N. Waterhouse, The roles of metal co-catalysts and reaction media in photocatalytic hydrogen production: Performance evaluation of M/TiO_2 photocatalysts (M=Pd, Pt, Au) in different alcohol–water mixtures, *J. Catal.*, 2015, **329**, 355–367.

31 P. Kalluru, G. A. B. Azizar, R. K. Pramadewandaru, T. G. Kim, J. Yu, D. I. Kang, J. Jung, Y. W. Lee and J. W. Hong, Synergistic function of Bi and B in interstitial ternary Pd–Bi–B alloy nanocrystals for highly active and durable electrochemical ethanol oxidation, *J. Mater. Chem. A*, 2025, **13**, 10019–10027.

32 Y. Wang, M. Zheng, Y. Li, C. Ye, J. Chen, J. Ye, Q. Zhang, J. Li, Z. Zhou, X.-Z. Fu, J. Wang, S.-G. Sun and D. Wang, p–d orbital hybridization induced by a monodispersed Ga site on a Pt_3Mn nanocatalyst boosts ethanol electrooxidation, *Angew. Chem., Int. Ed.*, 2022, **61**, e202115735.

33 Y. Liu, M. Wei, D. Raciti, Y. Wang, P. Hu, J. H. Park, M. Barclay and C. Wang, Electro-oxidation of ethanol using Pt_3Sn alloy nanoparticles, *ACS Catal.*, 2018, **8**, 10931–10937.

34 W. Trisap, S. Photaworn and P. Khongprom, Impact of hydrocyclone geometry on glycerol separation efficiency in biodiesel purification, *Int. J. Chem. Eng.*, 2025, **2025**, 1758062.

35 M. Simões, S. Baranton and C. Coutanceau, Electrochemical valorisation of glycerol, *ChemSusChem*, 2012, **5**, 2106–2124.

36 X. Tan, J. Wang, Y. Xiao, Y. Guo, W. He, B. Du, H. Cui and C. Wang, Engineering topological and chemical disorder in Pd sites for record-breaking formic acid electrocatalytic oxidation, *Adv. Mater.*, 2025, **37**, 2414283.

37 P. A. Kempler and A. C. Nielander, Reliable reporting of Faradaic efficiencies for electrocatalysis research, *Nat. Commun.*, 2023, **14**, 1158.

38 Y. Chen, J. Meng, M. Xu, L. Qiao, D. Liu, Y. Kong, X. Hu, Q. Liu, M. Chen, S. Lyu, R. Tong and H. Pan, Adaptive active site tuning for superior OER and UOR on Ir–Ni_3N catalyst, *Adv. Funct. Mater.*, 2025, **35**, 2413474.

39 S. Xu, X. Ruan, M. Ganesan, J. Wu, S. K. Ravi and X. Cui, Transition metal-based catalysts for urea oxidation reaction (UOR): Catalyst design strategies, applications, and future perspectives, *Adv. Funct. Mater.*, 2024, **34**, 2313309.

40 A. Kumar and Q. Xu, Two-dimensional layered materials as catalyst supports, *ChemNanoMat*, 2018, **4**, 28–40.

41 J. Choi, S. Im, J. Choi, S. Surendran, D. J. Moon, J. Y. Kim, J. K. Kim and U. Sim, Recent advances in 2D structured materials with defect-exploiting design strategies for electrocatalysis of nitrate to ammonia, *Energy Mater.*, 2024, **4**, 400020.

42 S. Roy, A. Joseph, X. Zhang, S. Bhattacharyya, A. B. Puthirath, A. Biswas, C. S. Tiwary, R. Vajtai and P. M. Ajayan, Engineered two-dimensional transition metal dichalcogenides for energy conversion and storage, *Chem. Rev.*, 2024, **124**, 9376–9456.

43 Q. Wang and D. O'Hare, Recent advances in the synthesis and application of layered double hydroxide (LDH) nanosheets, *Chem. Rev.*, 2012, **112**, 4124–4155.

44 M. Xu and M. Wei, Layered double hydroxide-based catalysts: Recent advances in preparation, structure, and applications, *Adv. Funct. Mater.*, 2018, **28**, 1802943.

45 M. Gong, Y. Li, H. Wang, Y. Liang, J. Z. Wu, J. Zhou, J. Wang, T. Regier, F. Wei and H. Dai, An advanced Ni–Fe layered double hydroxide electrocatalyst for water oxidation, *J. Am. Chem. Soc.*, 2013, **135**, 8452–8455.

46 W. Choi, N. Choudhary, G. H. Han, J. Park, D. Akinwande and Y. H. Lee, Recent development of two-dimensional transition metal dichalcogenides and their applications, *Mater. Today*, 2017, **20**, 116–130.

47 R. Yang, Y. Fan, Y. Zhang, L. Mei, R. Zhu, J. Qin, J. Hu, Z. Chen, Y. Hau Ng, D. Voiry, S. Li, Q. Lu, Q. Wang, J. C. Yu and Z. Zeng, 2D transition metal dichalcogenides for photocatalysis, *Angew. Chem., Int. Ed.*, 2023, **62**, e202218016.

48 H.-W. Choi, D. H. Seo, J. W. Heo, S.-I. Kim and T. Kim, Thickness-dependent electrical and optoelectrical properties of $SnSe_2$ field-effect transistors, *Electron. Mater. Lett.*, 2025, **21**, 154–161.

49 P. M. Bodhankar, P. B. Sarawade, G. Singh, A. Vinu and D. S. Dhawale, Recent advances in highly active nanostructured NiFe LDH catalyst for electrochemical water splitting, *J. Mater. Chem. A*, 2021, **9**, 3180–3208.

50 Y. Lin, H. Wang, C.-K. Peng, L. Bu, C.-L. Chiang, K. Tian, Y. Zhao, J. Zhao, Y.-G. Lin, J.-M. Lee and L. Gao, Co-induced electronic optimization of hierarchical NiFe LDH for oxygen evolution, *Small*, 2020, **16**, 2002426.

51 R. Yang, Y. Zhou, Y. Xing, D. Li, D. Jiang, M. Chen, W. Shi and S. Yuan, Synergistic coupling of CoFe-LDH arrays with NiFe-LDH nanosheet for highly efficient overall water splitting in alkaline media, *Appl. Catal., B*, 2019, **253**, 131–139.

52 S. Nagappan, A. Karmakar, R. Madhu, S. S. Selvasundarasekar, S. Kumaravel, K. Bera, H. N. Dhandapani, D. Sarkar, S. M. Yusuf and S. Kundu, 2D CoFe-LDH nanosheet-incorporated 1D microfibers as a high-performance OER electrocatalyst in neutral and alkaline media, *ACS Appl. Energy Mater.*, 2022, **5**, 11483–11497.

53 Q. Fu, J. Han, X. Wang, P. Xu, T. Yao, J. Zhong, W. Zhong, S. Liu, T. Gao, Z. Zhang, L. Xu and B. Song, 2D transition metal dichalcogenides: Design, modulation, and challenges in electrocatalysis, *Adv. Mater.*, 2021, **33**, 1907818.

54 R. Lv, J. A. Robinson, R. E. Schaak, D. Sun, Y. Sun, T. E. Mallouk and M. Terrones, Transition metal dichalcogenides and beyond: Synthesis, properties, and applications of single- and few-layer nanosheets, *Acc. Chem. Res.*, 2015, **48**, 56–64.

55 B. H. Kim, D. W. Kim, S. H. Kwon, H. Yoon and Y. J. Yoon, Contact and interface engineering of MoS_2-based photodetectors using electron-beam irradiation, *Electron. Mater. Lett.*, 2023, **19**, 564–570.

56 Z. Zheng, L. Yu, M. Gao, X. Chen, W. Zhou, C. Ma, L. Wu, J. Zhu, X. Meng, J. Hu, Y. Tu, S. Wu, J. Mao, Z. Tian and D. Deng, Boosting hydrogen evolution on MoS_2 via co-confining selenium in surface and cobalt in inner layer, *Nat. Commun.*, 2020, **11**, 3315.

57 B. Chamlagain, S. S. Withanage, A. C. Johnston and S. I. Khondaker, Scalable lateral heterojunction by chemical doping of 2D TMD thin films, *Sci. Rep.*, 2020, **10**, 12970.

58 M. Chhowalla, Z. Liu and H. Zhang, Two-dimensional transition metal dichalcogenide (TMD) nanosheets, *Chem. Soc. Rev.*, 2015, **44**, 2584–2586.

59 X. Ren, G. Liao, Z. Li, H. Qiao, Y. Zhang, X. Yu, B. Wang, H. Tan, L. Shi, X. Qi and H. Zhang, Two-dimensional MOF and COF nanosheets for next-generation optoelectronic applications, *Coord. Chem. Rev.*, 2021, **435**, 213781.

60 M. Nemiwal, T. C. Zhang and D. Kumar, Graphene-based electrocatalysts: Hydrogen evolution reactions and overall water splitting, *Int. J. Hydrogen Energy*, 2021, **46**, 21401–21418.

61 H. Wang and J.-M. Lee, Recent advances in structural engineering of MXene electrocatalysts, *J. Mater. Chem. A*, 2020, **8**, 10604–10624.

62 H. Kim, Multimodal MXene artificial synapses realizing optoelectronic, olfactory, and tactile neuromorphic memory in wearable devices, *Electron. Mater. Lett.*, 2025, 1–13.

63 Y. Zhang, X. Wang, M. Chen, P. He and Z. Kong, Two-dimensional leafy Fe/N-doped carbon nanomaterials derived from vitamin C-modified ZIF-L for efficient oxygen reduction reaction, *Electron. Mater. Lett.*, 2024, **20**, 592–602.

64 S. Jing, X. Peng, S. Li, L. Yuan, S. Lu, Y. Zhang and H. Fan, Synergistic realization of fast polysulfide redox kinetics and stable lithium anode in Li-S battery from CoNi-MOF/MXene derived CoNi@TiO_2/C heterostructure, *Chin. Chem. Lett.*, 2024, 110732.

65 C. S. Manikandababu, S. Navaneethan, M. I. S. Kumar, S. Ramkumar, K. Muthukannan and P. Siva Karthik, Construction of MoS_2@RGO hybrid catalyst: An efficient and highly stable electrocatalyst for enhanced hydrogen generation reactions, *Chem. Phys. Impact*, 2025, **10**, 100874.

66 A. Hanan, D. Shu, U. Aftab, D. Cao, A. J. Laghari, M. Y. Solangi, M. I. Abro, A. Nafady, B. Vigolo, A. Tahira and Z. H. Ibupoto, Co2FeO4@rGO composite: Towards trifunctional water splitting in alkaline media, *Int. J. Hydrogen Energy*, 2022, **47**, 33919–33937.

67 A. Hanan, F. Bibi, G. Elsa, A. Numan, R. Walvekar and M. Khalid, A comprehensive review of double transition metal MXene ($Mo_2Ti_2C_3Tx$) in energy storage, conversion, and harvesting, *Mater. Today Energy*, 2025, **51**, 101905.

68 M. N. Lakhan, A. Hanan, Y. Wang, H. K. Lee and H. Arandiyan, Integrated MXene and metal oxide electrocatalysts for the oxygen evolution reaction: Synthesis, mechanisms, and advances, *Chem. Sci.*, 2024, **15**, 15540–15564.

69 A. Hanan, H. T. A. Awan, F. Bibi, R. R. R. Sulaiman, W. Y. Wong, R. Walvekar, S. Singh and M. Khalid, MXenes and heterostructures-based electrocatalysts for hydrogen evolution reaction: Recent developments and future outlook, *J. Energy Chem.*, 2024, **92**, 176–206.

70 Q. Wang, Y. Cheng, H. B. Tao, Y. Liu, X. Ma, D.-S. Li, H. B. Yang and B. Liu, Long-term stability challenges and opportunities in acidic oxygen evolution electrocatalysis, *Angew. Chem., Int. Ed.*, 2023, **62**, e202216645.

71 Y. Tang, C. Yang, X. Xu, Y. Kang, J. Henzie, W. Que and Y. Yamauchi, MXene nanoarchitectonics: Defect-engineered 2D MXenes towards enhanced electrochemical water splitting, *Adv. Energy Mater.*, 2022, **12**, 2103867.

72 A. Iqbal, J. Hong, T. Y. Ko and C. M. Koo, Improving oxidation stability of 2D MXenes: Synthesis, storage media, and conditions, *Nano Convergence*, 2021, **8**, 9.

73 H. Li, N. Cheng, Y. Zheng, X. Zhang, H. Lv, D. He, M. Pan, F. Kleitz, S. Z. Qiao and S. Mu, Oxidation stability of nanographite materials, *Adv. Energy Mater.*, 2013, **3**, 1176–1179.

74 X. Gao, S. Zhang, P. Wang, M. Jaroniec, Y. Zheng and S.-Z. Qiao, Urea catalytic oxidation for energy and environmental applications, *Chem. Soc. Rev.*, 2024, **53**, 1552–1591.

75 S.-K. Geng, Y. Zheng, S.-Q. Li, H. Su, X. Zhao, J. Hu, H.-B. Shu, M. Jaroniec, P. Chen, Q.-H. Liu and S.-Z. Qiao, Nickel ferrocyanide as a high-performance urea oxidation electrocatalyst, *Nat. Energy*, 2021, **6**, 904–912.

76 L. Wang, Y. Zhu, Y. Wen, S. Li, C. Cui, F. Ni, Y. Liu, H. Lin, Y. Li, H. Peng and B. Zhang, Regulating the local charge distribution of Ni active sites for the urea oxidation reaction, *Angew. Chem., Int. Ed.*, 2021, **60**, 10577–10582.

77 Y. Chen, J. Ge, Y. Wang, X. Zhao, F. Zhang and X. Lei, Nanostructured $MoSe_2/NiSe_2$ electrocatalysts with heterojunctions for hydrogen evolution coupling urea oxidation, *ACS Appl. Nano Mater.*, 2024, **7**, 12091–12100.

78 Q. Lin, G. Nan, D. Fu and L. Xie, Oxygen evolution reaction on NiFe-LDH/(Ni,Fe)OOH: Theoretical insights into the effects of electronic structure and spin-state evolution, *Phys. Chem. Chem. Phys.*, 2025, **27**, 4926–4933.

79 M. Cai, Q. Zhu, X. Wang, Z. Shao, L. Yao, H. Zeng, X. Wu, J. Chen, K. Huang and S. Feng, Formation and stabilization of NiOOH by introducing α-FeOOH in LDH: Composite electrocatalyst for oxygen evolution and urea oxidation reactions, *Adv. Mater.*, 2023, **35**, 2209338.

80 J.-M. Huo, Y. Wang, J.-N. Xue, W.-Y. Yuan, Q.-G. Zhai, M.-C. Hu, S.-N. Li and Y. Chen, High-valence metal doping induced lattice expansion for M–FeNi LDH toward enhanced urea oxidation electrocatalytic activities, *Small*, 2024, **20**, 2305877.

81 T. Y. Burshtein, Y. Yasman, L. Muñoz-Moene, J. H. Zagal and D. Eisenberg, Hydrazine oxidation electrocatalysis, *ACS Catal.*, 2024, **14**, 2264–2283.

82 W. Zhu, A. Gandi Naidu, Q. Wu, H. Yan, M. Zhao, Z. Wang and H. Liang, Simultaneous electrocatalytic hydrogen production and hydrazine removal from acidic waste water, *Chem. Eng. Sci.*, 2022, **258**, 117769.

83 X. Fu, D. Cheng, A. Zhang, J. Zhou, S. Wang, X. Zhao, J. Chen, P. Sautet, Y. Huang and X. Duan, Ag–Ru interface for highly efficient hydrazine assisted water electrolysis, *Energy Environ. Sci.*, 2024, **17**, 2279–2286.

84 J. N. Coleman, M. Lotya, A. O'Neill, S. D. Bergin, P. J. King, U. Khan, K. Young, A. Gaucher, S. De, R. J. Smith, I. V. Shvets, S. K. Arora, G. Stanton, H.-Y. Kim, K. Lee, G. T. Kim, G. S. Duesberg, T. Hallam, J. J. Boland, J. J. Wang, J. F. Donegan, J. C. Grunlan, G. Moriarty, A. Shmeliov, R. J. Nicholls, J. M. Perkins, E. M. Grieveson, K. Theuwissen, D. W. McComb, P. D. Nellist and V. Nicolosi, Two-dimensional nanosheets produced by liquid exfoliation of layered materials, *Science*, 2011, **331**, 568–571.

85 J. Si, Q. Zheng, H. Chen, C. Lei, Y. Suo, B. Yang, Z. Zhang, Z. Li, L. Lei, Y. Hou and K. Ostrikov, Scalable production of few-layer niobium disulfide nanosheets via electrochemical exfoliation for energy-efficient hydrogen evolution reaction, *ACS Appl. Mater. Interfaces*, 2019, **11**, 13205–13213.

86 X. Cheng and Y. Tong, Interface coupling of cobalt hydroxide/molybdenum disulfide heterostructured nanosheet arrays for highly efficient hydrazine-assisted hydrogen generation, *ACS Sustainable Chem. Eng.*, 2023, **11**, 3219–3227.

87 Y. Zhu, Y. Chen, Y. Feng, X. Meng, J. Xia and G. Zhang, Constructing Ru–O–TM bridge in NiFe-LDH enables high current hydrazine-assisted H_2 production, *Adv. Mater.*, 2024, **36**, 2401694.

88 Q. Wang, J. Liu, W. Zhang, T. Li, Y. Wang, H. Li and A. Cabot, Branch-regulated palladium–antimony nanoparticles boost ethanol electro-oxidation to acetate, *Inorg. Chem.*, 2022, **61**, 6337–6346.

89 K. Elsaid, S. Abdelfatah, A. M. Abdel Elabsir, R. J. Hassiba, Z. K. Ghouri and L. Vechot, Direct alcohol fuel cells: Assessment of the fuel's safety and health aspects, *Int. J. Hydrogen Energy*, 2021, **46**, 30658–30668.

90 A. Ahmadi, H. Ebrahimifar and M. B. Askari, Alcohol electrooxidation on three-component NiO/La_2O_3/MWCNTs catalyst for DAFC application, *Electrochem. Commun.*, 2025, **176**, 107936.

91 H. Yang, C. Li, L. Lü, Z. Li, S. Zhang, Z. Huang, R. Ma, S. Liu, M. Ge, W. Zhou and X. Yuan, Electronegativity-induced cobalt-doped platinum hollow nanospheres with

high CO tolerance for efficient methanol oxidation reaction, *J. Colloid Interface Sci.*, 2025, **678**, 300–308.

92 W. Zhang, Y. Zhao, J. Li, Y. Miao, P. He, Z. Wu, Y. Zhang, G.-R. Xu and L. Wang, C–C bond cleavage driven by lattice oxygen during ethanol oxidation process, *Adv. Funct. Mater.*, 2025, 2421763.

93 B. Zhu, B. Dong, F. Wang, Q. Yang, Y. He, C. Zhang, P. Jin and L. Feng, Unraveling a bifunctional mechanism for methanol-to-formate electro-oxidation on nickel-based hydroxides, *Nat. Commun.*, 2023, **14**, 1686.

94 C. Li, H. Pang, R. Xu, J. Fan, E. Liu and T. Sun, CoFe-layered double hydroxide needles on MoS_2/Ni_3S_2 nanoarrays for applications as catalysts for hydrogen evolution and oxidation of organic chemicals, *ACS Appl. Nano Mater.*, 2024, **7**, 6449–6459.

95 S. Jiang, T. Xiao, C. Xu, S. Wang, H.-Q. Peng, W. Zhang, B. Liu and Y.-F. Song, Passivating oxygen evolution activity of NiFe-LDH through heterostructure engineering to realize high-efficiency electrocatalytic formate and hydrogen co-production, *Small*, 2023, **19**, 2208027.

96 Q. Qian, X. He, Z. Li, Y. Chen, Y. Feng, M. Cheng, H. Zhang, W. Wang, C. Xiao, G. Zhang and Y. Xie, Electrochemical biomass upgrading coupled with hydrogen production under industrial-level current density, *Adv. Mater.*, 2023, **35**, 2300935.

97 J. Bao, H. Sun, W. Yan, S. Liu, W. Xu, J. Fan, C. Zhan, W. Liu, X. Huang and N. Chen, Large-scalable CO-tolerant ultrathin $PtTe_2$ nanosheets for formic acid oxidation, *Small Methods*, 2025, 2402155.

98 X. Huang, M. Wang, H. Zhong, X. Li, H. Wang, Y. Lu, G. Zhang, Y. Liu, P. Zhang, R. Zou, X. Feng and R. Dong, Metal–phthalocyanine-based two-dimensional conjugated metal–organic frameworks for electrochemical glycerol oxidation reaction, *Angew. Chem., Int. Ed.*, 2025, **64**, e202416178.

99 H. Yu, W. Wang, Q. Mao, K. Deng, Z. Wang, Y. Xu, X. Li, H. Wang and L. Wang, Pt single atom captured by oxygen vacancy-rich NiCo layered double hydroxides for coupling hydrogen evolution with selective oxidation of glycerol to formate, *Appl. Catal., B*, 2023, **330**, 122617.

100 S. Zeng, D. Qu, H. Sun, Y. Chen, J. Wang, Y. Zheng, J. Pan, J. Cao and C. Li, Crystalline/amorphous interface engineering and d–sp orbital hybridization synergistically boosting the electrocatalytic performance of PdCu bimetallene toward formic acid-assisted overall water splitting, *ACS Appl. Mater. Interfaces*, 2024, **16**, 64797–64806.

101 S. Hu, Y. Tan, C. Feng, H. Wu, J. Zhang and H. Mei, Synthesis of N doped NiZnCu-layered double hydroxides with reduced graphene oxide on nickel foam as versatile electrocatalysts for hydrogen production in hybrid-water electrolysis, *J. Power Sources*, 2020, **453**, 227872.

102 K. Xiang, Y. Wang, Z. Zhuang, J. Zou, N. Li, D. Wang, T. Zhai and J. Jiang, Self-healing of active site in $Co(OH)_2$/MXene electrocatalysts for hydrazine oxidation, *J. Mater. Sci. Technol.*, 2024, **203**, 108–117.

103 W. Liu, J. Xie, Y. Guo, S. Lou, L. Gao and B. Tang, Sulfurization-induced edge amorphization in copper–nickel–cobalt layered double hydroxide nanosheets promoting hydrazine electro-oxidation, *J. Mater. Chem. A*, 2019, **7**, 24437–24444.

104 J. Li, Y. Li, J. Wang, C. Zhang, H. Ma, C. Zhu, D. Fan, Z. Guo, M. Xu, Y. Wang and H. Ma, Elucidating the critical role of ruthenium single atom sites in water dissociation and dehydrogenation behaviors for robust hydrazine oxidation-boosted alkaline hydrogen evolution, *Adv. Funct. Mater.*, 2022, **32**, 2109439.

105 F. Sun, J. Qin, Z. Wang, M. Yu, X. Wu, X. Sun and J. Qiu, Energy-saving hydrogen production by chlorine-free hybrid seawater splitting coupling hydrazine degradation, *Nat. Commun.*, 2021, **12**, 4182.

106 M. Hao, J. Chen, J. Chen, K. Wang, J. Wang, F. Lei, P. Hao, X. Sun, J. Xie and B. Tang, Lattice-disordered high-entropy metal hydroxide nanosheets as efficient precatalysts for bifunctional electro-oxidation, *J. Colloid Interface Sci.*, 2023, **642**, 41–52.

107 G. Wang and Z. Wen, Self-supported bimetallic Ni–Co compound electrodes for urea- and neutralization energy-assisted electrolytic hydrogen production, *Nanoscale*, 2018, **10**, 21087–21095.

108 A. Nadeema, V. Kashyap, R. Gururaj and S. Kurungot, $[MoS_4]^{2-}$-intercalated NiCo-Layered double hydroxide nanospikes: An efficiently synergized material for urine to direct H_2 generation, *ACS Appl. Mater. Interfaces*, 2019, **11**, 25917–25927.

109 Y. Feng, X. Wang, J. Huang, P. Dong, J. Ji, J. Li, L. Cao, L. Feng, P. Jin and C. Wang, Decorating CoNi layered double hydroxides nanosheet arrays with fullerene quantum dot anchored on Ni foam for efficient electrocatalytic water splitting and urea electrolysis, *Chem. Eng. J.*, 2020, **390**, 124525.

110 C. Gu, G. Zhou, J. Yang, H. Pang, M. Zhang, Q. Zhao, X. Gu, S. Tian, J. Zhang, L. Xu and Y. Tang, NiS/MoS_2 Mott-Schottky heterojunction-induced local charge redistribution for high-efficiency urea-assisted energy-saving hydrogen production, *Chem. Eng. J.*, 2022, **443**, 136321.

111 Y. Ren, C. Wang, W. Duan, L. Zhou, X. Pang, D. Wang, Y. Zhen, C. Yang and Z. Gao, MoS_2/Ni_3S_2 Schottky heterojunction regulating local charge distribution for efficient urea oxidation and hydrogen evolution, *J. Colloid Interface Sci.*, 2022, **628**, 446–455.

112 C. Li, Y. Liu, Z. Zhuo, H. Ju, D. Li, Y. Guo, X. Wu, H. Li and T. Zhai, Local charge distribution engineered by Schottky heterojunctions toward urea electrolysis, *Adv. Energy Mater.*, 2018, **8**, 1801775.

113 Z. Wang, W. Liu, J. Bao, Y. Song, X. She, Y. Hua, G. Lv, J. Yuan, H. Li and H. Xu, Modulating electronic structure of ternary NiMoV LDH nanosheet array induced by doping engineering to promote urea oxidation reaction, *Chem. Eng. J.*, 2022, **430**, 133100.

114 S. Wang, L. Zhao, J. Li, X. Tian, X. Wu and L. Feng, High valence state of Ni and Mo synergism in NiS_2-MoS_2 hetero-nanorods catalyst with layered surface structure for urea electrocatalysis, *J. Energy Chem.*, 2022, **66**, 483–492.

115 Z. Wang, Y. Hu, W. Liu, L. Xu, M. Guan, Y. Zhao, J. Bao and H. Li, Manganese-modulated cobalt-based layered double hydroxide grown on nickel foam with 1D–2D–3D heterostructure for highly efficient oxygen evolution reaction and urea oxidation reaction, *Chem. – Eur. J.*, 2020, **26**, 9382–9388.

116 Y. Zheng, P. Tang, X. Xu and X. Sang, POM derived UOR and HER bifunctional NiS/MoS_2 composite for overall water splitting, *J. Solid State Chem.*, 2020, **292**, 121644.

117 M. Li, X. Deng, K. Xiang, Y. Liang, B. Zhao, J. Hao, J.-L. Luo and X.-Z. Fu, Value-added formate production from selective methanol oxidation as anodic reaction to enhance electrochemical hydrogen cogeneration, *ChemSusChem*, 2020, **13**, 914–921.

118 X. Peng, S. Xie, X. Wang, C. Pi, Z. Liu, B. Gao, L. Hu, W. Xiao and P. K. Chu, Energy-saving hydrogen production by the methanol oxidation reaction coupled with the hydrogen evolution reaction co-catalyzed by a phase separation induced heterostructure, *J. Mater. Chem. A*, 2022, **10**, 20761–20769.

119 Y. Zhang, X. Wu, G. Fu, F. Si, X.-Z. Fu and J.-L. Luo, NiFexP@NiCo-LDH nanoarray bifunctional electrocatalysts for coupling of methanol oxidation and hydrogen production, *Int. J. Hydrogen Energy*, 2022, **47**, 17150–17160.

120 H. Wang, L. Wang, Y. Jia, X. Li, H. Yang, X. Zhu, Q. Bu and Q. Liu, Engineering lattice planes of NiCo-LDH ultrathin sheets for boosting methanol/ethanol oxidation performance, *Inorg. Chem.*, 2023, **62**, 11256–11264.

121 B. Liu, T. Xiao, X. Sun, H.-Q. Peng, X. Wang, Y. Zhao, W. Zhang and Y.-F. Song, Hierarchical trace copper incorporation activated cobalt layered double hydroxide as a highly selective methanol conversion electrocatalyst to realize energy-matched photovoltaic-electrocatalytic formate and hydrogen co-production, *J. Mater. Chem. A*, 2022, **10**, 19649–19661.

122 M. Li, X. Deng, Y. Liang, K. Xiang, D. Wu, B. Zhao, H. Yang, J.-L. Luo and X.-Z. Fu, Co_xP@NiCo-LDH heteronanosheet arrays as efficient bifunctional electrocatalysts for co-generation of value-added formate and hydrogen with less-energy consumption, *J. Energy Chem.*, 2020, **50**, 314–323.

123 T. T. Huynh, Q. Huynh, A. Q. K. Nguyen and H. Q. Pham, Strong component-interaction in N-doped 2D Ti_3C_2T-supported Pt electrocatalyst for acidic ethanol oxidation reaction, *Adv. Sustainable Syst.*, 2025, **9**, 2400995.

124 L. Xu, Z. Wang, X. Chen, Z. Qu, F. Li and W. Yang, Ultrathin layered double hydroxide nanosheets with Ni(III) active species obtained by exfoliation for highly efficient ethanol electrooxidation, *Electrochim. Acta*, 2018, **260**, 898–904.

125 H. Wang, M. Huo, Y. Liang, K. Qin, Q. Li, W. Liu, Z. Xing and J. Chang, Significant reduction of anode reaction overpotential in alkaline water electrolysis by ultrathin NiFe-layered double hydroxide in ethanol-added electrolyte, *ChemCatChem*, 2025, **17**, e202401950.

126 L. Wang, J. Qi, Y. Zhang, Y. Dai, K. Bao, W. Wang, J. Wu, C. Ma, Z. Yin, C. Ma, Y. Chen, J. Bao, R. Ye, Y. Liu, Z. Lin, Z. Wang and Q. He, Surface engineering of $PtSe_2$ crystal for highly efficient electrocatalytic ethanol oxidation, *Adv. Mater.*, 2025, **37**, 2502047.

127 Z. Chen, F. Jing, M. Luo, X. Wu, H. Fu, S. Xiao, B. Yu, D. Chen, X. Xiong and Y. Jin, Local coordination and electronic interactions of Pd/MXene via dual-atom codoping with superior durability for efficient electrocatalytic ethanol oxidation, *Carbon Energy*, 2024, **6**, e443.

128 C. Yang, H. He, Q. Jiang, X. Liu, S. P. Shah, H. Huang and W. Li, Pd nanocrystals grown on MXene and reduced graphene oxide co-constructed three-dimensional nanoarchitectures for efficient formic acid oxidation reaction, *Int. J. Hydrogen Energy*, 2021, **46**, 589–598.

129 C. Yang, H. Pang, X. Li, X. Zheng, T. Wei, X. Ma, Q. Wang, C. Wang, D. Wang and B. Xu, Scalable electrocatalytic urea wastewater treatment coupled with hydrogen production by regulating adsorption behavior of urea molecule, *Nano-Micro Lett.*, 2025, **17**, 159.

130 Z. Li, Y. Zheng, W. Zu, L. Dong and L. Y. S. Lee, Molybdate-modified NiOOH for efficient methanol-assisted seawater electrolysis, *Adv. Sci.*, 2025, **12**, 2410911.

131 G. Qian, T. Lu, Y. Wang, H. Xu, X. Cao, Z. Xie, C. Chen and D. Min, N-induced compressive strain in Ni-MoO_2 heterostructure with micro-nano array for improving high-current-output urea-assisted water electrolysis performance, *Chem. Eng. J.*, 2024, **480**, 147993.

132 B. Zhu, J. Xiong, S. Wu, K. You, B. Sun, Y. Liu, M. Chen, P. Jin and L. Feng, Core@Shell heterostructured $NiMoP_x$@Ni_5P_4 nanorod arrays promoting direct electro-oxidation of methanol and hydrogen evolution under industry conditions, *Adv. Funct. Mater.*, 2024, **34**, 2407236.

133 S. M. Hu, Y. N. Chen, J. K. Liu, X. Y. Zhang, W. H. Jiang, Y. Zhou, H. Y. Yuan, P. F. Liu, Q. Guo, H. G. Yang, F. Wang and G. Yu, Inhibiting the peroxidation of Co(III) oxyhydroxide for stable and ampere-level glycerol oxidation, *Appl. Catal., A*, 2026, **381**, 125811.

134 S. Im, D. Kim, S. Surendran, J. Choi, D. J. Moon, J. Y. Kim, H. Lee, D.-H. Nam and U. Sim, High entropy alloy: From theoretical evaluation to electrocatalytic activity of hydrogen evolution reaction, *Curr. Opin. Electrochem.*, 2023, **39**, 101293.

135 D. Kim, S. Surendran, Y. Jeong, Y. Lim, S. Im, S. Park, J. Y. Kim, S. Kim, T.-H. Kim, B. Koo, K. Jin and U. Sim, Electrosynthesis of low Pt-loaded high entropy catalysts for effective hydrogen evolution with improved acidic durability, *Adv. Mater. Technol.*, 2023, **8**, 2200882.

136 J. Cavin, A. Ahmadiparidari, L. Majidi, A. S. Thind, S. N. Misal, A. Prajapati, Z. Hemmat, S. Rastegar, A. Beukelman, M. R. Singh, K. A. Unocic, A. Salehi-Khojin and R. Mishra, 2D high-entropy transition metal dichalcogenides for carbon dioxide electrocatalysis, *Adv. Mater.*, 2021, **33**, 2100347.

137 Z. Wang, X. Chen, Y. Ding, X. Zhu, Z. Sun, H. Zhou, X. Li, W. Yang, J. Liu, R. He, J. Luo, T. Yu, M. Zeng and L. Fu, Synthesis of two-dimensional high-entropy transition metal dichalcogenide single crystals, *J. Am. Chem. Soc.*, 2025, **147**, 1392–1398.

138 S. K. Nemani, M. Torkamanzadeh, B. C. Wyatt, V. Presser and B. Anasori, Functional two-dimensional high-entropy materials, *Commun. Mater*, 2023, **4**, 16.

139 J. Qu, A. Elgendy, R. Cai, M. A. Buckingham, A. A. Papaderakis, H. de Latour, K. Hazeldine, G. F. S. Whitehead, F. Alam, C. T. Smith, D. J. Binks, A. Walton, J. M. Skelton, R. A. W. Dryfe, S. J. Haigh and D. J. Lewis, A Low-temperature synthetic route toward a high-entropy 2D hexernary transition metal dichalcogenide for hydrogen evolution electrocatalysis, *Adv. Sci.*, 2023, **10**, 2204488.

140 F. Wang, P. Zou, Y. Zhang, W. Pan, Y. Li, L. Liang, C. Chen, H. Liu and S. Zheng, Activating lattice oxygen in high-entropy LDH for robust and durable water oxidation, *Nat. Commun.*, 2023, **14**, 6019.

141 S. K. Nemani, B. Zhang, B. C. Wyatt, Z. D. Hood, S. Manna, R. Khaledialidusti, W. Hong, M. G. Sternberg, S. K. R. S. Sankaranarayanan and B. Anasori, High-entropy 2D carbide MXenes: $TiVNbMoC_3$ and $TiVCrMoC_3$, *ACS Nano*, 2021, **15**, 12815–12825.

142 Y. Ying, K. Fan, Z. Lin and H. Huang, Facing the "Cutting Edge:" Edge site engineering on 2D materials for electrocatalysis and photocatalysis, *Adv. Mater.*, 2025, **37**, 2418757.

143 A. Shaban, M. E. Basiouny and O. A. AboSiada, Comparative study of the removal of urea by electrocoagulation and electrocoagulation combined with chemical coagulation in aqueous effluents, *Sci. Rep.*, 2024, **14**, 30605.

144 Y. Chen, H. Chen, Z. Chen, Z. Zhu and X. Wang, The nitrogen removal performance and mechanisms for urea wastewater by simultaneous urea hydrolysis, partial nitritation and anammox in one reactor, *J. Cleaner Prod.*, 2022, **332**, 130124.

145 Z. Wu, M. Fan, H. Jiang, J. Dai, K. Liu, R. Hu, S. Qin, W. Xu, Y. Yao and J. Wan, Harnessing the unconventional cubic phase in 2D $LaNiO_3$ perovskite for highly efficient urea oxidation, *Angew. Chem., Int. Ed.*, 2025, **64**, e202413932.

146 P. Mannu, R. K. Dharman, T. T. T. Nga, A. Mariappan, Y.-C. Shao, H. Ishii, Y.-C. Huang, A. Kandasami, T. H. Oh, W.-C. Chou, C.-L. Chen, J.-L. Chen and C.-L. Dong, Tuning of oxygen vacancies in Co_3O_4 electrocatalyst for effectiveness in urea oxidation and water splitting, *Small*, 2025, **21**, 2403744.

147 Y. Wang, G. Qian, Z. Xie, H. Yu, L. Li, J. Li, C. Chen, M. Lu and P. Tsiakaras, Strengthening CuNiCoMo medium-entropy alloy by tuning local lattice tensile strain and built-in electric field for boosting urea oxidation reaction, *Appl. Catal., B*, 2025, **365**, 124841.

148 P. Wang, X. Gao, M. Zheng, M. Jaroniec, Y. Zheng and S. Z. Qiao, Urine electrooxidation for energy–saving hydrogen generation, *Nat. Commun.*, 2025, **16**, 2424.

149 H. Qin, G. Lin, J. Zhang, X. Cao, W. Xia, H. Yang, K. Yuan, T. Jin, Q. Wang and L. Jiao, Enhanced cooperative generalized compressive strain and electronic structure engineering in W-Ni_3N for efficient hydrazine oxidation facilitating H_2 production, *Adv. Mater.*, 2025, **37**, 2417593.

150 M. Akhtar, M. Sarfraz, M. Ahmad, N. Raza and L. Zhang, Use of low-cost adsorbent for waste water treatment: Recent progress, new trend and future perspectives, *Desalin. Water Trea*, 2025, **321**, 100914.

151 P. Rajasulochana and V. Preethy, Comparison on efficiency of various techniques in treatment of waste and sewage water – A comprehensive review, *Resour.-Effic. Technol.*, 2016, **2**, 175–184.

152 T. Yu, G. Liu, T. Nie, Z. Wu, Z. Song, X. Sun and Y.-F. Song, Pt-loaded CoFe-layered double hydroxides for simultaneously driving HER and HzOR, *ACS Catal.*, 2024, **14**, 14937–14946.